# Dynamics and statics of actin assemblies

by

Jennifer Hyunjong Shin

Submitted to the Department of Mechanical Engineering
in partial fulfillment of the requirements for the degree of
Doctor of Philosophy in Mechanical Engineering
at the
MASSACHUSETTS INSTITUTE OF TECHNOLOGY
February 2004



Author .....
Department of Mechanical Engineering
February 6, 2004

Certified by .....
L. Mahadevan
Gordon McKay Professor of Applied Mathematics and Mechanics,
DEAS, Harvard University
Thesis Supervisor

Certified by .....
Paul Matsudaira
Professor of Biology, Bioengineering and Environmental Science
Thesis Supervisor

Certified by .....
Peter So
Thesis Committee Chairman, Professor of Mechanical Engineering
Thesis Supervisor

Accepted by .....
Ain A. Sonin
Chairman, Departmental Committee on Graduate Students
Department of Mechanical Engineering

# Dynamics and statics of actin assemblies

by

Jennifer Hyunjong Shin

Submitted to the Department of Mechanical Engineering
on February 6, 2004, in partial fulfillment of the
requirements for the degree of
Doctor of Philosophy in Mechanical Engineering

## Abstract

The conversion of chemical energy into mechanical forces that powers cell movements is a ubiquitous theme across biology. The acrosome reaction of *Limulus* sperm is a simple example of such a dynamical transformation where a 60 $\mu$m-long crystalline bundle of actin filaments, tightly cross-linked by actin bundling protein scruin, straightens from a coiled conformation and extends from the cell in five seconds. This spring-like mechanism represents a third type of actin-based motility that is distinctly different from the better known polymerization or myosin-driven processes. To identify the basis and mechanism for this movement, we examine the possible sources of chemical and mechanical energy and show that the stored elastic energy alone is sufficient to drive the reaction. We also provide an estimate of the maximum force generated during the uncoiling by stalling the bundle using an agarose gel. Finally, we provide a simple mathematical model that rationalizes the dynamics of uncoiling.

Motivated by the very stiff cross-linking in the bundle induced by scruin, we next turn to a model system of scruin mediated cross-linked actin networks where the elastic response is dominated by the properties of actin. While the biological significance of the actin cross-linking proteins is well documented, little is known about how bundling and cross-linking quantitatively affects the microstructure and mechanical properties of actin networks. We quantify the effect of scruin on actin networks using imaging techniques, co-sedimentation assays, multi-particle tracking (MPT), and bulk rheology and demonstrate how a simple entropic elasticity model for a semi-flexible polymer network explains the linear elastic regime of the actin-scruin network.

Thesis Supervisor: L. Mahadevan
Title: Gordon McKay Professor of Applied Mathematics and Mechanics, DEAS, Harvard University

Thesis Supervisor: Paul Matsudaira
Title: Professor of Biology, Bioengineering and Environmental Science

Thesis Supervisor: Peter So
Title: Thesis Committee Chairman, Professor of Mechanical Engineering

# Acknowledgments

First of all, I would like to thank Professor L. Mahadevan and Professor Paul Matsudaira for offering me a great opportunity to work with them and introducing me this spectacular problem in biophysics presented in this thesis. I thank both my advisors for their sincere advice of independence and self-confidence in my thoughts and actions. They patiently waited and guided me with consistent trust and encouragement while I was making my rough entrance to the field of biophysics with my limited background. I also thank both Professor So and Professor van Oudenaarden for their support and advice during my Ph.D research.

It has been a great pleasure to work with people in the Matsudaira Lab at the Whitehead Institute. I first thank Barney Tam for being such a wonderful friend and for his help in various experiments. I also thank Guichy Waller, Lera Baru, Winston Timp and all other lab members for their encouragement and advice during my hard moments. I am grateful to Tom Canal and Ketsada Syhakhom for their friendly assistance with administrative matter. Special thanks go to Professor Dave Weitz and members in his lab. Especially I would like to acknowledge Margaret Gardel, who has been a great collaborator and a good friend, sharing hardships and laughs for last three years.

My thanks go to Ms. Leslie Regan for her excellent administrative assistance and for patiently waiting for this thesis to be finalized.

I would also like to send warmest regard and appreciation to my friends who supported me for last two years. Very special thanks go to Dr. Ho-Young Kim who always encouraged and helped me in my lowest moments. His sincere care, harsh advice, and faithful love made it possible for me to continue and not give up when I tumbled down exhausted.

Finally, last but not least, I would like to acknowledge my parents with my greatest thanks and love. I also send my love and thanks to my wonderful sisters, brothers-in-law, and my nine dearest nephews and nieces.

*God, I thank you for your words of promise that led me this far.* **"So do not fear, for I am with you; do not be dismayed, for I am your God. I will strengthen you and help you; I will uphold you with my righteous right hand." Isaiah 41:10**

# Contents

# List of Figures

5-5 **Derivation of elasticity of a semi-flexible polymer** (A) A single inextensible semi-flexible filament with a contour length of $l_c$: (a) at absolute zero temperature (T=0) where thermal effects vanish, the end-to-end distance, $l$, of a semi-flexible polymer equals to $l_c$. (b) for T>0, the filament undergoes thermal fluctuation of a magnitude $h$, and $l$ contracts by $\Delta'$ due to the thermal bending such that $l = l_c - \Delta'$. The corresponding bending energy is $U_B \sim \kappa_0 l(h/l^2)^2$ where $\kappa_0$ is the filament bending rigidity. (c) In the presence of an applied extensional force, $F$, the contracted filament extends by $\delta$ with the stretching energy of $U_F \sim Fl\varepsilon \sim Fh^2/l$ where $\varepsilon$ is the net stain of the filament due to both the bending and stretching, $\varepsilon = (\Delta' - \delta)/l_c$. The elastic energy due to bending and stretching must balance the thermal energy by equipartition such that $U_B + U_F \sim (\kappa/l^2 + F)\varepsilon l \sim k_B T$. This can be re-written for $\varepsilon \sim (l^2/l_p - Fl^4/k_B T l_p^2)/l_c$ with the persistence length, $l_p = \kappa/k_B T$, yielding the lateral displacements $\Delta' \sim l^2/l_p$ and $\delta \sim Fl^4/k_B T l_p^2$; thus, the linear force-extension is $F \sim (\kappa^2/k_B T l^4)\delta$. (B) For a cross-linked network characterized by a pore size $\xi$, the stress $\sigma$ is defined by $\sigma \sim F/\xi^2$ and the imposed strain is $\gamma \sim \delta/l_c$ where $l_c$ is now the distance between cross-links. This leads to the network elastic modulus $G' \sim \sigma/\gamma \sim \kappa^2/(k_B T \xi^2 l_c^3)$. . . . . 91

# List of Tables

# Chapter 1

# Introduction

## 1.1 Background and motivation

### 1.1.1 Actin and actin binding proteins

Actin is one of the most ubiquitous and highly conserved proteins in eukaryotic cells. It exists either as a globular monomer (G-actin) or as a filament (F-actin). G-actin readily polymerizes under physiological conditions to form a double-helical F-actin with the simultaneous hydrolysis of ATP. F-actin plays an important role in maintaining the mechanical integrity of eukaryotic cells. The elastic modulus of cytoplasmic actin gels is estimated to be of the order of 100 - 1000 Pa [16] and the gel must be able to sustain shear stresses of up to 1000 Pa for proper cell function [4]. Yet, a solution of pure actin filaments alone at its concentration of 23.8 $\mu$M (1mg/ml) is a weak elastic solid with a low frequency elastic modulus of only 0.1 Pa. The pure actin filaments relax past each other under a shear stress of as little as 0.1 Pa, resulting in a rapid decrease in modulus [18, 20]. To be suited for their functional role as cytoskeletal and motility components in cells, actin filaments associate into bundles or networks in concert with more than 60 different actin binding proteins (ABPs) enhancing their rigidity and elasticity. Organizing individual actin filaments into higher order structures is controlled by bivalent actin-binding proteins [27]. ABPs that possess at least two actin-binding sites are able to connect different subunits of actin, either within

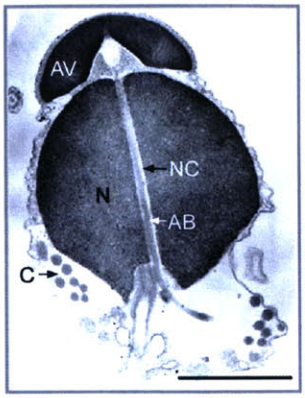


Figure 1-1: A cross-sectional electron micrograph of an un-reacted *Limulus* sperm, showing the proximal end of the acrosomal bundle (AB) lying in the nuclear channel (NC) while the rest of the bundle coiled around the base of the nucleus (N) (shown as 6-7 circular cross-sections (C)). Upon activation by the presence of an egg or $Ca^{2+}$, the acrosomal bundle uncoils and extends out through a narrow channel at a constant velocity.

a single filament or between neighboring filaments. In the latter case, the F-actin can form a cross-linked gel or a parallel bundle depending on the length and rigidity of the region between the two actin-binding domains in the ABPs. In disordered gels, a flexible ABP, such as filamin, connect neighbouring filaments to form a loosely cross-linked orthogonal arrays and the viscoelastic nature of the networks provides cells with structural rigidity. In ordered bundles, the filaments are aligned axially in compact parallel arrays by small ABPs (e.g., fascin or fimbrin) that force the close alignment, providing stiffness within long thin processes such as neurosensory bristle of Drosophila [58, 56, 6], brush border microvilli [19] and hair cell stereocilia [59, 54].

In this work, we are interested in an actin binding protein, scruin, that is uniquely found in the acrosomal process of *Limulus polyphemus* (horseshoe crab) sperm. Scruin, a 102 kDa hetero-dimeric protein with a 16kDa calmodulin in its neck region, decorates an individual F-actin and scruin-scruin interactions lead to both cross-linking and bundling of neighbouring actin filaments. *In vivo*, scruin mediates the formation of a single ordered crystalline bundle of over 80 actin filaments which functions as a mechanical spring during the acrosomal reaction of the horseshoe crab sperm. *In vitro*, actin filaments polymerized in the presence of scruin are cross-linked and bun-

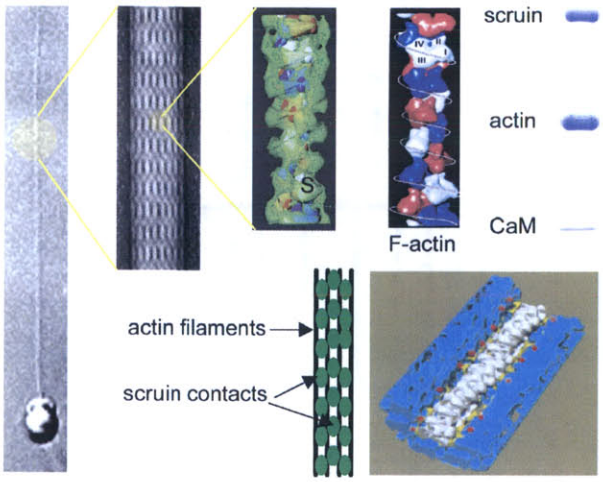


Figure 1-2: Composition of the acrosomal bundle: The acrosomal bundle is a crystalline bundle made of three proteins, scruin:CaM (calmodulin) complex (120kDa) and actin (42kDa) (shown in the right-most image of an SDS-PAGE gel). Scruin (S) (indicated as green cloud) decorates actin filaments at 1:1 stochiometric ratio and more than 50 scruin decorated filaments form a rigid bundle via various scruin-scruin interactions (high-lighted in yellow in the bottom image taken from Schmid et al.).

dled by scruin contacts and form an isotropic, disordered three-dimensional network. The goal of this work is to understand the dynamics and statics of both ordered and disordered actin assemblies composed of identical constituent proteins, actin, scruin, and CaM.

### 1.1.2 *In vivo* dynamic actin bundle in *Limulus* sperm

The acrosome reaction of the sperm of the horseshoe crab *Limulus polyphemus* is an unusual example of actin-based motility. In an un-reacted sperm cell, a bundle of actin is preformed as a coil of 6 loops wrapping around the base of the nucleus (see Fig. 1-1). Upon contact with the egg jelly-coat or in a calcium rich environment, a bundle of actin filaments cross-linked by scruin:CaM heterodimers extends from the head of the sperm through a nuclear channel to form a 60 $\mu$m-long finger of membrane, termed the acrosomal process [53].

The acrosomal process consists of up to 80 actin filaments tightly cross-linked by scruin. The electron microscopy (EM)-derived structure shows that the acrosomal

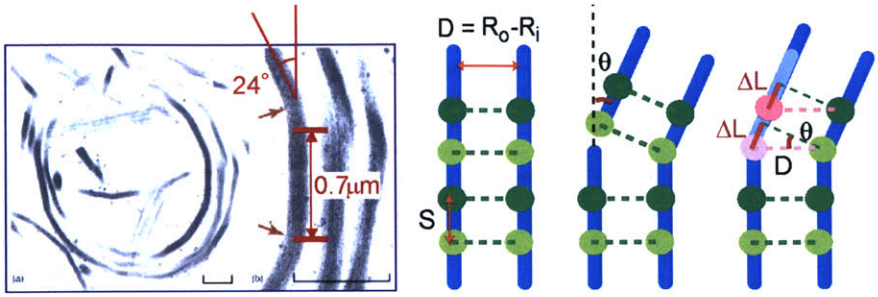


Figure 1-3: (a) Electron micrograph of a sperm cross-section shows that the coil features 14 discrete arms and elbows. Each elbow is 0.7 $\mu$m long and makes 156° between arms. (b) A schematic representation of cross-linking between adjacent filaments shows scruin-scruin contacts in green circular dots and two adjacent actin filaments in blue. Given that two inter-filament spacing (D) is 133Å and the distance (S) between two cross-links is 55Å, if we suppose that we want to form a kink of an angle $\theta$ with no breaking or stretching allowed in the filaments, the filaments must slide by $\Delta L = S$ such that scruin contacts are still in register between adjacent filaments. $\Delta L = D\mathtt{sin}\theta$ leads to $\theta \sim \mathtt{sin}^{-1}(S/D) \sim 24°$. This kink angle $\theta$ of 24° determines number of arms and elbows in the loop, which is 14. Moreover, two adjacent monomers of 0.23° twist are 27Å apart, and thus in order to have 60° superhelicity, we will need about 260 subunits of actin monomers per filament, which corresponds to about 0.7 $\mu$m distance between two adjacent kinks. Since there are 14 segments of 0.7 $\mu$m per loop, it gives rise to a circumference of about 10 $\mu$m, yielding a diameter of 3.2 $\mu$m for the coil.

process is an extensively cross-linked bundle of actin filaments in which scruin cross-links are spaced along every actin subunit with its stoichiometric ratio of 1:1 (scruin dimer: actin monomer) (Sanders et al., 1996) (see Fig. 1-2). Helical reconstructions of a filament [42] show that scruin is a bi-lobed protein, which decorates the outside of actin filaments. Two domains in scruin lie across the actin filament axis and cross-links pairs of neighbouring actin subunits along the filament. Schmid model [42] shows that scruin binds pairs of actin subunits in the same filament with one lobe of scruin binding to subdomain 1 of one actin subunit while the other lobe binding to subdomain 3 of an adjacent actin subunit. Scruin then makes a variety of non-identical contacts with neighbouring scruin molecules on different filaments to form a tight crystalline bundle.

While most other actin-based bundles are known to have one or two cross-linking proteins per more than ten actin subunits [12], the acrosomal bundle features very

dense amount of scruin, which may be a key factor in forming a stiff and regular crystalline structure. In addition to being a very stiff crystalline bundle, the acrosomal bundle shows a few unique and remarkable features, which will further explain (1) how the long bundle is packed into a small confined space inside the sperm cell, (2) how the coil is transformed to a straight bundle, and finally (3) how the bundle stores energy to power the reaction.

First of all, as shown in Fig. 1-3, each loop of the coil contains 14 discrete arms and elbows instead of being a smooth continuous circle. Secondly, the actin bundle is a right-handed superhelix with 60° per arm. Lastly, each filament is slightly over-twisted by 0.23° per subunit. These three geometrical factors are all inter-related to one another, and together they provide answers to the proposed questions above. Supposing that we try to bend this composite bundle into a coil, the bundle experiences lattice mismatch between filaments on the inner curve and ones on the outer curve. Since no compression or extension of the filaments is observed in the bundle, there must be some slippage between actin filaments relative to one another. Therefore, if we force the filaments pass through an elbow, each actin filament in the bundle will experience difference in its path length. However, having a 60° superhelicity in the bundle around the elbow of 156° angle ensures that (1) the individual filaments passing through the elbow cover the equal contour length in the coil, and (2) there is no indefinite accumulation of slippage along the filaments but rather an oscillating feature of slippage and cross-bridges [11]. Since the monomers are interconnected by cross-linking, this macroscopic superhelical conformation arises from the small microscopic overtwist of 0.23° per each subunit. As illustrated in Fig. 1-3 (b), two adjacent monomers in a 0.23° twisted filament are 27Å apart; in order to have 60° superhelicity between two adjacent kinks, we will need about 260 subunits of actin monomers per filament, which corresponds to about 0.7 $\mu$m distance between two adjacent kinks. Since there are 14 segments of 0.7 $\mu$m per loop, it gives rise to a circumference of about 10 $\mu$m, yielding a diameter of 3.2 $\mu$m for the coil. Therefore, the kinks, along with over-twisting and superhelicity, are essential for packing a 60 $\mu$m long bundle into a sperm cell of $\sim 3\mu$m diameter. Moreover, having the kinks enables the bundle

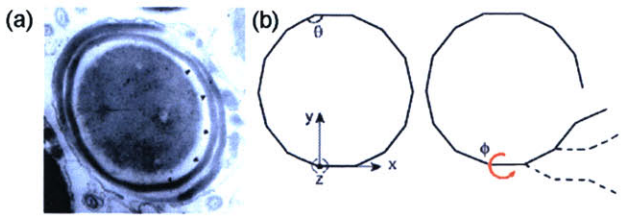


Figure 1-4: (a) A thin section electron micrograph of a sperm cross-section shows that the bundle is bent discretely (indicated with arrowheads) with a series of arms separated by elbows. (b) In going from the coil to the TD, the bundle has to rotate through an angle $\phi$ ($\phi = \pi$ in this drawing) at each arm. As the untwisting front propagates along the bundle, it extends out eventually forming a zigzag shape. This unusual design shows how nature uses kinks to convert one form of movement (untwisting) into another (extension)

to concentrate the energy in the kinks, which is more favorable because the bending energy scales with the length of the bundle while the energy of the kinks scale with the number of them.

We now turn to the question on how this packed coil straightens out to a true discharge (TD) form. As illustrated in Fig. 1-4, in going from a kinked coil to a straight TD, the bundle must unwind the superhelix and rotate through an angle $\phi$ per each arm. As the untwisting front propagates along the bundle, it extends out to eventually form a zig-zag shapes. Additional rotation about z-axis by $\theta$ must then follow to obtain a straight bundle. Due to the 60° superhelicity per arm, the bundle has a total of 2.3 turns around its long axis for each loop of coil. Due to this feature, one should expect the extending bundle to make a total 14-15 revolutions during the reaction; in fact this rotational motion is easily observed when the tip of the bundle is buckled (see Fig. 1-5). Finally, the 0.23° over-twisting per subunit of actin filaments is putatively the basis for storing energy and driving the extension of the bundle [11]. Considering that individual actin filaments in their unbound form are known to have about 5-6 angular disorder per subunit [14], it is very possible that the modest fluctuations in the twist of actin subunits are captured and frozen-in by scruin since the degree of twist in the *Limulus* bundle is well within the range of their random variable twist [15]. This small difference in twist between subunits is amplified by the polymeric assembly of the filament over-twisting of the actin filaments, causing high

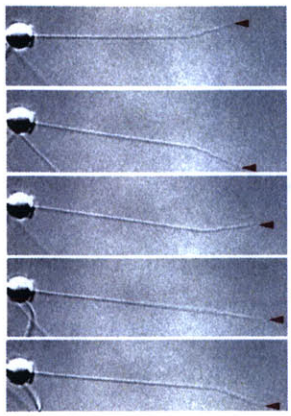

Figure 1-5: Selected frames in the sequence of the acrosomal process show that bundle rotates as it extends, and for each revolution, the tip advances by $\sim 4.3\mu$m. Total of 14-15 revolutions corresponds to the total degree of the superhelicity being unwound during the extension.

stress and strain on the filaments for a possible energy storage.

To meet its functional goal to penetrate an egg in the absence of external chemical fuelling, the acrosomal process in the *Limulus* sperm is built with these remarkable structural features. During the uncoiling process, the untwisting of the bundle is accompanied by slippage between filaments and untwisting of the individual actin filaments, leading to the conversion of the coil to its straight form. In doing so, mechanical potential energy stored in the coil is converted into translational work. Therefore, *in vivo*, scruin mediated crystalline bundle of actin filaments functions as a dynamic mechanical spring, representing a third type of actin-based motility that is distinctly different from the better known polymerization or myosin-driven processes. Our goal is to understand the energetics and forces involved in this dynamic transformation of an actin bundle.

### 1.1.3 *In vitro* static actin networks

Motivated by stiff cross-linking in the acrosomal bundle, we now turn to the *in vitro* system of actin:scruin complex. Unlike the ordered *in vivo* actin bundle found in the *Limulus* sperm, actin filaments polymerized in the presence of scruin form an isotropic, disordered three-dimensional semi-flexible network of cross-linked and bun-

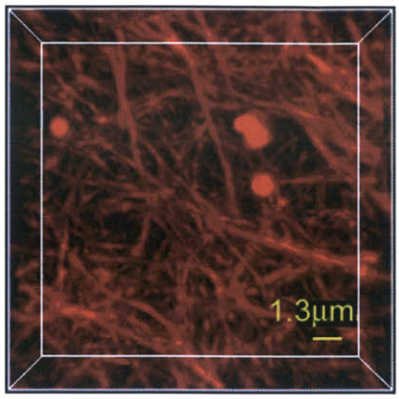


Figure 1-6: Confocal image of a 1:1 (scruin:actin) bundled and cross-linked network of actin:scruin composite *in vitro*. Circular red dots are embedded particles of 100nm diameter.

dled F-actin (see Fig. 1-6). These disordered networks often exhibit a complex relationship between their macroscopic mechanical properties and the elastic properties of the constituent filaments. While the biological significance of the actin cross-linking proteins is well documented, little is known about how bundling and cross-linking quantitatively affects the microstructure and mechanical properties of actin networks. Moreover, the scruin-actin composite network is a model system in studying the physics of cross-linked semi-flexible polymer networks whose elastic response is dominated by that of actin. Therefore, it allows a remarkable tunability in the elastic behavior upon addition of rigid cross-links, leading to striking variety in the linear and nonlinear elastic response.

## 1.2 Organization of thesis

Chapter 1 describes the background and motivation for the study of dynamics and statics of actin assemblies. In chapter 2, we investigate the dynamic actin assembly found in the horseshoe crab sperm by considering various energy sources and sinks involved in the system and provide estimates for each. [1] Chapter 3 offers two independent measurements of the bending stiffness of an isolated crystalline bundle of

[1]Published in *Journal of Cell Biology*, 2003, 162: 1183-1188

actin, using a steady flow and a single pole magnetic trap.[2] In chapter 4, we present a direct measurement of the force the acrosomal process generates during the reaction by means of (1) stalling the acrosomal reaction in an agarose gel and (2) mechanically slowing down in highly viscous media. Finally, in chapter 5, motivated by the tight cross-linking in scruin mediated in vivo assemblies, we construct an *in vitro* system of actin:scruin composite network and relate the structural studies to its mechanical response via theoretical models for semi-flexible polymer networks. [3] Chapter 6 offers the conclusions of this thesis with suggestions for future directions.

[2]Published in *Journal of Molecular Biology*, 2003, 337(2): 255-261
[3]Submitted in *PNAS*, 2003

# Chapter 2

# Stored elastic energy powers the 60 $\mu$m extension of the *Limulus polyphemus* sperm actin bundle

## 2.1 Introduction

The acrosome reaction of the sperm of the horseshoe crab *Limulus polyphemus* is an unusual example of actin-based motility. Upon contact with the egg jelly-coat, a bundle of actin filaments cross-linked by scruin:CaM heterodimers extends from the head of the sperm through a nuclear channel to form a 60 $\mu$m-long finger of membrane, the acrosomal process. The reaction requires the presence of $Ca^{2+}$ ions and is completed in about five seconds (see Fig. 2-1). However, because the bundle is preformed as a coil around the base of the nucleus and does not contain myosin, extension of the membrane must involve a different mechanism for generating force than polymerization or molecular motor-based processes. Based on structural analysis of the actin bundle before and after activation, DeRosier and Tilney suggested that the movement was driven by a spring-like mechanism in which mechanical energy is stored in the conformation of the coiled bundle [13]. The structure of the coiled bundle is unlike any known actin structure Fig. 2-2. In contrast to the typical linear conformation of actin bundles in microvilli or filopodia, the coiled state consists of 6 polygonal loops. Each loop is made of 14 straight segments connected by kinks at 0.7 $\mu$m intervals [12]. In addition to the polygonal structure of the bundle, the bundle exhibits a 60° superhelical twist per segment, which gives rise to 14-15 revolutions

along the entire bundle, thus allowing different filaments to cover equivalent distances in a coil. This macroscopic helical packing conformation arises due to the small microscopic overtwist of 0.23° per each subunit, and is putatively the basis for storing energy and driving the extension of the bundle [11]. This small difference in twist between subunits, which represents a relatively large twisting strain of approximately 85.4°/$\mu$m [12] is amplified by the polymeric assembly of the filament into almost two additional turns over the 106 subunits along the length of the bundle. During the acrosome reaction, the filaments untwist, bends melt, and the coil rotates and straightens to a true discharge (TD) state [12, 13]. The change in actin twist coupled to the uncoiling of the polygonal bundle is postulated to be the motive force for extension of the bundle.

## 2.2 Materials and Methods

### 2.2.1 Sample preparations

#### Sperm and acrosome isolation

Sperm were collected by stimulating the gonopores of *Limulus polyphemus* males. Cells were centrifuged twice at 750 g for 5 minutes and resuspension in artificial seawater (ASW: 423mM NaCl, 9mM KCl, 9.27mM $CaCl_2$, 22.94mM $MgCl_2$, 25.5mM $MgSO_4$, 2.15mM $NaHCO_3$, 10mM Tris, pH adjusted to 8.0) to be stored as a pellet on ice. The TD state was prepared following Sanders, et al. [41]. The FD state was prepared following Tilney [53] but with the minor modification that the FD was induced by suspending the washed sperm in 5 volumes of 0.1 % Triton X-100, 0.1mM EDTA, 3mM $MgCl_2$, 30mM Tris at pH 8 (4°C).

### 2.2.2 Imaging

#### Light microscopy

The acrosome reaction was induced by diluting the sperm suspension with 25mM $CaCl_2$ to a 1:100 (vol:vol $CaCl_2$:ASW). Calcium ionophore A23187 (1mg/ml in DMSO) was diluted 1:10 with 25mM $CaCl_2$. The experiments were conducted in a flat cap-

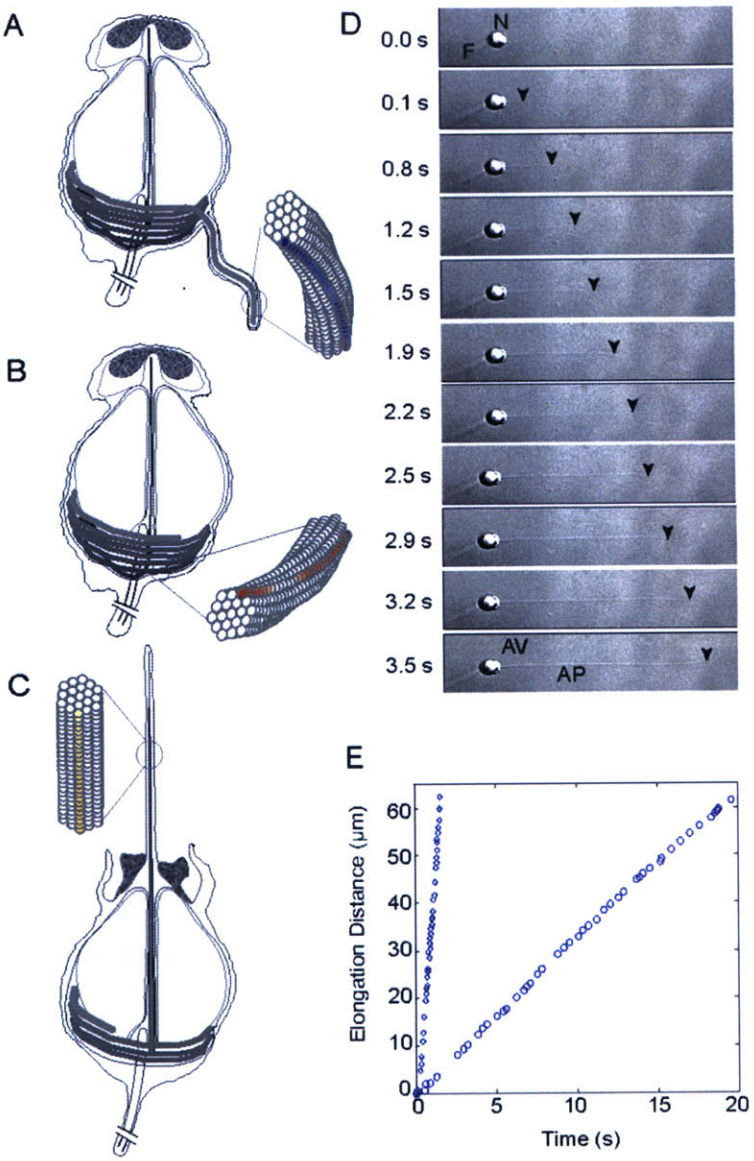


Figure 2-1: A schematic of *Limulus* sperm based on electron micrographs. The filaments are twisted both in the (a) coiled state and (b) FD state with opposite chirality; the filaments are free of twists in the (c) TD state. During the acrosomal reaction, going from the coil to the true discharge, the actin filaments untwist and unbend. The reaction occurs at a constant velocity (d, e).

illary flow cell (18 mm×6 mm×0.3 mm) constructed from a glass coverslip sealed to a glass microscope slide with Apiezon grease. A sperm suspension was introduced into the flow cell with a pipette and left to adhere to the coverslip. The acrosome reaction was induced with a flow of A23187. Cells were imaged under DIC-H optics at 100×magnification on a Nikon TE300 inverted microscope, captured by a Hamamatsu Orca CCD video camera, and digitized at 30 fps using an Apple Video player.

### 2.2.3 Biochemical measurements

#### Nucleotide identification (courtesy of G.Waller K. Lansetmo)

To identify the nucleotide present in the acrosomal process, TD and FD were isolated, washed several times with 50mM Tris at pH 8.6 (4°C), and dialyzed of free nucleotide. Solid urea was added to washed pellets to a final concentration of 8M in a final volume of 200 $\mu$l to extract the bound nucleotide. Samples were incubated at room temperature for at least 1 hour, diluted to 3.2 ml with 50mM Tris at pH 8.6 and centrifuged at 349,000 g for 20 minutes (Beckman TLA). The extracts were applied at a flow rate of 0.25 ml/min to a 1-ml TOYOPEARL DEAE-650S ion exchange column equilibrated in 50 mM Tris at pH 8.6. AMP, ADP, and ATP eluted with a gradient of 0-1M NaCl in 50mM Tris at pH 8.6. The positions of peaks were monitored at 254 nm and compared with the elution times and peak areas of AMP, ADP, ATP, GMP, GDP, and GTP nucleotide standards (Sigma, Inc) in separate runs under identical conditions. Chromatography was performed at 4°C.

#### Calorimetry (courtesy of G.Waller K. Lansetmo)

To measure $Ca^{2+}$ binding to purified acrosomes, trace levels of $Ca^{2+}$ were reduced by washing plasticware and glassware with 1M HCl. $Ca^{2+}$-free buffer (150 mM KCl, 25 mM HEPES pH 7.5, 3 mM NaN3) was prepared by passing the sample through a CHELEX 100 column. $Ca^{2+}$ was removed from acrosome suspensions by overnight dialysis at 5°C against $Ca^{2+}$-free buffer containing 0.5 % CHELEX 100 resin (200-400 mesh, BioRad, Inc.) and then against two changes of $Ca^{2+}$-free buffer alone. $Ca^{2+}$ solutions were prepared from a 0.1M stock solution of a $Ca^{2+}$ standard (Orion)

diluted with 150 mM KCl, 25 mM HEPES pH 7.5, 3mM NaN3. $Ca^{2+}$ binding to TD and FD acrosomes was measured by isothermal titration calorimetry using a Microcal VP-ITC instrument. Aliquots of a $Ca^{2+}$ solution, typically 0.25 mM $CaCl_2$ in 150 mM KCl, 25 mM HEPES pH 7.5, 3mM NaN3 were injected into the calorimetry cell and the heat released was measured. Data was analyzed using Microcal Origin software and was fitted assuming 4 sequential $Ca^{2+}$ binding sites.

## 2.3 Results and Discussions

To understand how the acrosomal process extends, we examined the relative contributions of the mechanical and chemical potentials to the free energy change that accompanies the reaction. We first estimate the stored elastic strain energy in the twisted bundle by treating it as an initially straight, isotropic, elastic rod of circular cross-section (the hexagonal packing of the filaments allows this as a reasonable first approximation) that is uniformly twisted. For such a rod, the elastic stored energy is [28]

$$U \approx \int \frac{1}{2}(A\kappa^2 + C\tau^2)ds \tag{2.1}$$

where $A$ is the bending stiffness and $\kappa$ the curvature of the bundle, $C$ the twisting stiffness, $\tau$ the twist per unit length, and $L$ the total length of the bundle. Based on this relationship, we can estimate the stored energy with the measured values of the bending and twisting stiffness. Electron micrographs reveal that the bundle is sharply bent at 0.7 $\mu$m intervals (see Fig. 2-2). The large curvature about the kinks extends over a length of the order of the thickness of the bundle; over this distance the filaments slip relative to each other just like in tilt-boundaries in crystalline materials [38]. Since the energy of the kinks scales sub-linearly with the length of the local bend, this energy is small. In contrast to having a discrete number of bends, the coiled bundle is continuously twisted over its entire length. Since the energy associated with kinks is small, the stored elastic energy in Eq. 2-1 may then be well approximated by

$$U \approx \int C\tau^2 L/2 \tag{2.2}$$

For an isotropic rod with a circular cross-section, $A=3C/2$, a good estimate of the twisting stiffness $C$ may be derived from the bending stiffness $A$, which is much easier to measure. We estimate the bending stiffness of the acrosome bundle from the shape of the bent bundle when subjected to a steady hydrodynamic flow at low Reynolds numbers (see Chapter 3), and find it to be $A \approx 5\times10^{-21}$ Nm$^2$ ($5\times10^9$ pN$\cdot nm^2$), leading to a persistence length of $l_p \approx A/k_BT \approx 1.2$m. The total stored elastic energy is then $U \approx A\tau^2$L$/3\approx 3\times10^{-13}$J ($7\times10^7$k$_B$T), and is much larger than the energy in the kinks. Indeed the kinks are important geometrically; they pack the bundle into the sperm in an energetically efficient manner and convert twist into extension during unpacking [11], not being the primary energy source for the reaction. Evidence of this is seen in experiments where the kinks sometimes do not melt leading to a kinked TD (see Fig. 2-2). Thus, the acrosome reaction can be thought of as a two step process: (i) the primary event wherein the bundle untwists and extends, with the kinks converting (un)twist to extension (ii) the secondary event wherein the kinks melt, although this does not have to always follow.

Although mechanical energy is clearly responsible for large movements of macromolecular assemblies, energy may also be contributed by two other obvious energy sources, hydrolysis of ATP by actin and the energy released by $Ca^{2+}$ binding. In a typical filament, the bound nucleotide in an actin subunit is ADP. However, it is conceivable that delayed hydrolysis of ATP could be coupled to extension of the bundle. Thus we determined the state of bound nucleotide in the false discharge (FD) form (see Fig. 2-1) of the acrosomal bundle by ion exchange column chromatography. The nucleotide status of the FD is measured for two reasons. First, the coiled bundles cannot be purified with any degree of biochemical purity and isolated coils are always contaminated with small fragments of FD. Secondly, the FD is a valid model of the coil because the two forms are rapidly and reversibly inter-convertible in live cells [2]. Because a cell can spontaneously extend and retract a FD within a few minutes, it is unlikely that the coil has a bound nucleotide different than the FD. Based on the

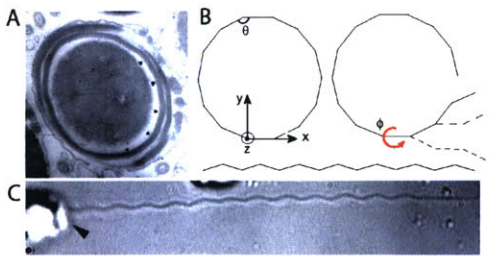


Figure 2-2: Uncoiling of bent and twisted rods (A) A thin section electron micrograph of a sperm cross-section shows that the bundle is bent discretely (indicated with arrowheads) with a series of arms separated by elbows, allowing the 60 $\mu$m bundle to be snugly packed in a 5 $\mu$m sperm. (B) In going from the coil to the TD, the bundle has to rotate through an angle $\phi$ ($\phi = \pi$ in this drawing) at each arm. As the untwisting front propagates along the bundle, it extends out eventually forming a zigzag shapes. This unusual design shows how nature uses kinks to convert one form of movement (untwisting) into another (extension). (C) In rare occasions, the second rotation about the z-axis does not occur, resulting in a zigzag kinked TD. The arrowhead points the ruptured acrosomal vesicle, which ensures that what we see is the TD coming out of the apical end of the sperm head.

elution volumes and peak areas of known amounts of injected nucleotide standards, the extracted nucleotide from both the TD and FD states is ADP. ATP is not detected in either preparation. Furthermore, the stoichiometry of extracted ADP to actin is 1.2:1 (mole:mole). Thus, the coiled bundle most likely consists of ADP-actin subunits (see Fig. 2-3).

A second more probable source of chemical energy is the energy released by $Ca^{2+}$ binding to the bundle. From thermodynamics, the energy of $Ca^{2+}$ binding is simply the difference between the energy of binding to the coil and to the TD [67]. The sole $Ca^{2+}$ binding sites in the bundle reside in the single CaM subunit of scruin:CaM heterodimers. To measure $Ca^{2+}$ binding energy, we measured the heat of $Ca^{2+}$ binding to the TD and FD forms of the bundle by isothermal titration calorimetry. In control experiments with isolated horseshoe crab CaM and scruin:CaM complexes, $Ca^{2+}$ bound to four sites in the heterodimer. However, in the isolated actin bundle of the TD or FD, only two $Ca^{2+}$ binding sites were detected (see Table 2-1).

From the heat of binding we derive an association constant and finally a Gibbs free energy. The calculated difference in energy of binding to the FD and TD at 25°C is $3.6\times10^{-15}$ J ($8.8\times10^{5}k_BT$ ). This value, an upper bound on the available free

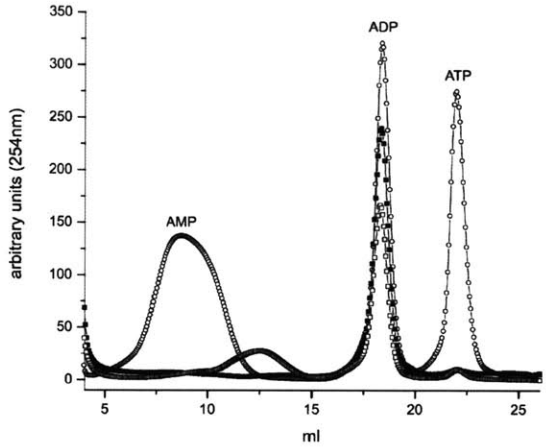


Figure 2-3: Chromatographs of nucleotides eluted from an ion exchange column. AMP, ADP, and ATP display elution volumes of 7 ml, 18.5 ml, and 22 ml. Nucleotides extracted from the true (solid squares) and false (open squares) are identified as predominantly ADP when compared with nucleotide standards (open circles). The minor peak at 12.5 ml is unidentified.

Table 2.1: Thermodynamic parameters for $Ca^{2+}$ binding determined by isothermal titration calorimetry. K and $\Delta$H for the binding of each $Ca^{2+}$ are determined by a nonlinear least squares fit of the data. For *limulus* sperm calmodulin (CaM) and scruin data are fit using a sequential binding model with four sites. Averages and deviations for five (CaM) and two (scruin) experiments are presented. For true discharge (TD) and false discharge (FD), the two high affinity $Ca^{2+}$ binding sites do not have different thermal properties, and were therefore fit using a single site model with a stoichiometry of two. Averages and deviations for three (TD) and two (FD) experiments are presented on a per $Ca^{2+}$ basis. Binding of $Ca^{2+}$ to the two low affinity sites of TD and FD was not observed. Units for $K_n$ and $\Delta H_n$ are $M^{-1} \times 10^6$ and $kcal \cdot mol^{-1}$, respectively.

| Protein | $K_1$ | $\Delta H_1$ | $K_2$ | $\Delta H_2$ | $K_3$ | $\Delta H_3$ | $K_4$ | $\Delta H_4$ |
|---|---|---|---|---|---|---|---|---|
| CaM | .36±.2 | -1.6±.5 | .16±.1 | .3±.7 | .26±.1 | -4.5±.5 | 6±4.4 | -1.8±1 |
| Scruin | 2.4±.6 | -1.9±.8 | 1.9±.4 | -2.9±.2 | 2.1±.2 | 1.9±.3 | 3.2[a] | -1.8±.5 |
| TD | 1.7±.8 | 2.5±.4 | 1.7±.8 | -2.5±.4 | NO[b] | NO | NO | NO |
| FD | 2.5±.4 | -3.1±.1 | 2.5±.4 | -3.1±.1 | NO | NO | NO | NO |

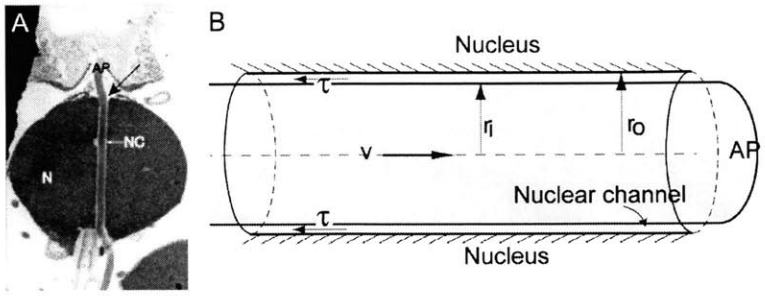


Figure 2-4: Hydrodynamic dissipation in the channel. (A) Thin section electron micrograph of an extending acrosomal bundle shows that the acrosomal process (AP, also indicated with a black arrow) passes through a very tight nuclear channel (NC). (B) The acrosomal bundle moving through a nuclear channel is represented schematically. As the bundle passes through a narrow channel, it experiences a shear force $\tau$.

energy of $Ca^{2+}$ binding, is almost two orders of magnitude smaller than the lower bound estimate of the elastic energy. Our measurements of sources of mechanical and chemical energy show that there is ample elastic energy to extend the acrosomal process.

Having considered the sources of energy, we now briefly turn to a discussion of the energy sinks in the system. Just as the bundle is able to store a substantial amount of energy in twist, it dissipates this energy as it untwists in a viscous environment. Once the scruin-actin bond is loosened, the untwisting of the filaments leads to shearing between them as is clear from electron-micrographs of the different states of the bundle [11]. This leads to a dissipation that can potentially be very large owing to the high degree of confinement that magnifies the shear rate for purely geometric reasons since this geometric magnification is much larger than that in the nuclear channel.

As the bundle extends, it experiences friction in the highly viscous environment. The nuclear channel is very narrow, and the clearance between the channel wall and the bundle surface is only of the order of a few nm (while the average diameter of the bundle is approximately 100nm). Due to this small clearance between the bundle and the channel wall, hydrodynamic dissipation outside the channel is much smaller than the dissipation in the channel (see Fig. 2-4). The rate of the hydrodynamic dissipation due to shearing inside the narrow channel can be estimated from $\dot{E} \approx \int \eta(\nabla u)^2 dV$

where $\eta$ is the viscosity of the cytoplasm ($\eta$= 0.01 Pa, conservatively estimated to be ten times that of water), $\nabla u$ the velocity gradient between the nuclear channel wall and the moving acrosome (typically $\nabla u \sim \nu/(r_o - r_i)$), and $V$ the volume over which dissipation occurs, $V \sim r_i(r_o - r_i)L$. We calculate the dissipation rate to be $4\times10^{-17}$W ($10^4\ k_BT/s$) based on the average velocity $v\sim$ 15$\mu$m/s, the average bundle radius $r_i \sim 0.05\mu$m, the average clearance between the channel and the acrosome, $r_o - r_i\sim 0.005\mu$m, and the length of the nuclear channel, $L\sim 5\mu$m. For the average duration t$\sim$ 5 seconds, the total energy dissipated is $\dot{E}t \sim 10^{-15}$J ($2.4\times10^5\ k_BT$). It must be emphasized that this estimate of dissipated energy, which is nearly three orders of magnitude smaller than the estimated stored elastic energy, provides only a lower bound on the energy required to drive the reaction. Since the velocity of uncoiling changes by nearly an order of magnitude when the temperature is changed by less than 15 %, the rate-limiting step cannot be the viscous resistance of the nuclear channel. Energy may also be consumed as the acrosomal bundle pushes or stretches the membrane during the reaction. However, Tilney [55] showed that the outer nuclear envelope surrounding the coil is converted into the 18 $\mu$m$^2$ of new plasma membrane surrounding the TD. Thus the membrane is unlikely to be a significant energy sink. We speculate that most of the energy is dissipated by inter-filament sliding as the bundle untwists (see Fig. 2-5).

Cellular engines that power motility usually fall into two categories: polymerization ratchets and molecular motors. The work performed by both types of engines depends on continual hydrolysis of ATP. Here we provide quantitative evidence to support a third type of cellular engine, a spring, in which the energy is stored in the conformation of the actin:scruin complex in the coiled bundle using a subtle combination of geometric packing and chemical binding. We base this conclusion on three pieces of evidence. First, the acrosomal actin bundle is stiff and requires enormous energy to bend and twist into a coil; we estimate the elastic energy to be approximately $10^{-13}$J ($2.5\times10^7\ k_BT$). To place this number in perspective, we compare the specific power of the acrosome with other force-generating engines. A single bundle contains $10^6$ subunits of actin and scruin and a mass $\sim 2\times10^{-16}$kg [41]. From the

combined bending and twisting energy, the specific power is $2.5\times10^2$ J/s. This value is two orders of magnitude smaller than the specific power of an ATP-driven motor protein and of the same order of magnitude as the bacterial rotary motor, striated muscle, and a gasoline automobile engine [31] suggesting that it has sufficient power as a cellular engine for motility. Second, a typical actin-based engine requires expenditure of chemical energy to do work [29]. However, we rule out the possibility that ATP hydrolysis is directly coupled to the acrosome reaction because the FD and TD contain ADP in a 1:1 molar ratio with actin. Because the coil can reversibly convert into a FD, the bound nucleotide of the coil is most likely ADP. The third piece of evidence is the low yield of work from $Ca^{2+}$ binding. Although the energy from ligand binding could power the movement, our measurements show that the energy released from $Ca^{2+}$ binding to the TD and FD is insufficient by two orders of magnitude to account for the mechanical energy expended in the reaction. Thus, based on our measurements of mechanical and chemical energy, we conclude that there is ample elastic energy but not chemical energy to extend the acrosomal process.

How conformational changes store energy is unknown but the stiffness measurements and three-dimensional reconstructions of the TD suggest a possible clue. The electron microscopy (EM)-derived structure shows that the TD is an extensively crosslinked bundle of actin filaments in which scruin crosslinks are spaced along every actin subunit [42, 47]. In contrast, a more conventional actin bundle fimbrin-crosslinked actin filaments [57, 62], crosslinks are spaced 36 nm along an actin filament. The difference in stiffness between the acrosomal bundle and a fimbrin-type bundle arises because they differ in the density of protein crosslinks between filaments. Based on the measured bending stiffness and an average bundle radius of $r$ ~50 nm yields a Young's modulus $E{=}4A/R^4{\sim}$ $10^9$ Pa for the composite actin-scruin bundle, comparable to that of a stiff elastomer and similar to that of pure actin filaments [26]. The Young's modulus is consistent with the 3D structure of the acrosomal bundle which is closer to a solid rod of protein than a braid of filaments separated by water-filled space. The close association between neighbouring filaments inferred from the mechanical properties and the biochemical studies of scruin suggests that scruin is a

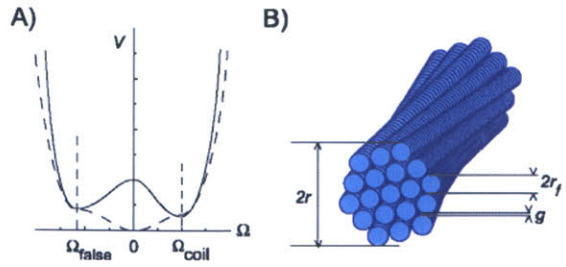


Figure 2-5: Theoretical model: We consider each cross-section of the bundle. Initially, there are two possible stable states of the bundle: the coil and false-discharge states, which have opposite chiralities (A). They are separated by the true-discharge state that is unstable in the absence of calcium, as shown via the solid line in (A). Once calcium binds to the scruin-CaM complex, the scruin undergoes a conformation change that causes the actin filaments, originally in their twisted state to be released. Then, the potential well is modified and is converted to the dashed line in (A), wherein the true discharge becomes the globally stable state. This leads to an untwisting of the cross-section which then propagates as a front along the bundle. To understand the dynamics of this front, we remind ourselves that the driving force is due to the elastic stresses in the twisted bundle, while the dissipation is dominated by the shearing between the individual filaments as schematically indicated in (B). The balance of twisting torques then leads to the following equation for the twisting strain $\Omega(x,t)$ as a function of location along the bundle $x$ at time t: $\alpha\frac{\partial\Omega}{\partial t} = -\frac{\partial}{\partial x}(\frac{\partial V}{\partial\Omega}) + \gamma^2\frac{\partial^2\Omega}{\partial x^2}$ where $\alpha$ is the drag coefficient associated with inter filament shearing, and $\gamma$ is the coupling coefficient that penalizes sharp changes in the twist along the bundle, and $V$ is the potential associated with the scruin-actin complex. Looking for travelling wave solutions of the form reduces the equation to a simple ordinary differential equation that can be solved analytically [32]

latch that holds actin filaments and the acrosomal bundle in their unusual conformations. It also explains how changes to the twist of individual filaments are physically coupled to inter-filament shearing during the formation and release of the TD [32]. Recent structural and biochemical studies [41, 42, 47] are consistent with the hypothesis that the scruin-CaM complex undergoes a conformation change in the presence of $Ca^{2+}$ allowing the twisted actin filaments to untwist relative to each other.

Formally there are two possibilities for the uncoiling mechanism. In an unzipping model, a spatially localized zone of conformational change propagates between the two phases of the acrosome so that only a segment of the bundle uncoils at one time. In this scenario, which is similar to other polymorphic transitions in supramolecular systems [21], we expect the actin bundle to extend with a nearly constant velocity. In contrast, a global explosion model involves uncoiling throughout the entire bundle,

with the nuclear channel converting the change into motion. In this model, the extension velocity of the acrosome would decrease exponentially with time after a short explosive initial transient. Experimental results indicate that the velocity of extension is constant during the reaction, supporting the model where the local untwisting propagates spontaneously along the bundle once a critical threshold is reached; equivalently the region remains fixed in space while the bundle moves through this region sequentially uncoiling section by section. Since the energy from $Ca^{2+}$ binding is at least 100-fold lower than the expended mechanical energy, our studies suggest that $Ca^{2+}$ is a trigger that initiates the reaction, which is then self-sustained and driven by the stored elastic energy.

This dynamical event is analogous to a phase transition in a crystalline material [39], which allows for conformation changes to occur in a localized zone of activity (a defect, dislocation or front) where the material is transformed from one ordered phase (twisted) to another (untwisted). A simple analogy that illustrates the role of localized zones of activity may be found by considering the motion of a heavy carpet on the ground. It can be moved by (a) pulling it so that it slides uniformly, (b) by forming a small localized fold that is then forced to roll along the carpet. Clearly, the latter is energetically more efficient, but requires some energy to nucleate a fold before it can propagate under the influence of, say gravity. Just as in the context of a carpet, a critical size of the untwisted phase for the actin bundle must be nucleated by some environmental factors. Our experiments suggest that $Ca^{2+}$ binding triggers the reaction by changing the relative energy of the different states of the bundle. In particular, it makes the initially unstable straight state stable relative to the coiled state. Once this critical event has occurred, we hypothesize that the reaction proceeds without any further need for $Ca^{2+}$, and is driven by the stored mechanical energy as the stable phase (the untwisted, unstrained bundle) invades an unstable phase (the twisted, strained bundle). In a long specimen, this front will travel with a nearly constant velocity determined by the balance between the driving force and the dissipation, i.e. the bundle should untwist with a nearly constant velocity. The conversion of twist to extension is achieved in a remarkable way in this

system, and uses the presence of kinks [12, 11]. Thus, the kinks are an efficient way of packing and unpacking the bundle, while the twisting strain is an efficient way of storing energy. A quantitative model requires further characterization of the problem parameters, and constitutes work currently in progress [32].

The coiled *Limulus* acrosomal bundle is not unique in storing elastic energy via small conformation changes in a crystalline protein biopolymer. Other examples include the tubulin assemblies in microtubules, virus capsids and clathrin coats, and bacterial flagella [39, 5, 69]. In these structures, small changes at the subunit level are amplified by the repetitive polymeric structure into large-scale movements. In principle, any polymeric structure is capable of storing elastic energy.

# Chapter 3

# Bending stiffness of the *in vivo* crystalline actin bundle

## 3.1 Introduction

Actin filaments, which play an important role in maintaining the mechanical integrity of eukaryotic cells, rarely exist independently. Actin filaments rarely exist as individual single filaments in cells. Instead, they normally associate into bundles or networks in concert with more than 60 different actin binding proteins (ABPs) to influence cellular shape, mitotic division, cell adhesion, and motility [27]. In networks, the filaments are loosely cross-linked in orthogonal arrays and its viscoelastic nature provides cells with structural rigidity. In bundles, the filaments form compact parallel arrays with rigid proteins that force the close alignment, providing stiffness. Examples of these stiff bundles are found in long thin processes such as the neuro-sensory bristle of Drosophila [58, 56, 6], the brush border microvilli [34], the hair cell stereocilia [59, 54], and the acrosomal process of *Limulus* sperm [47]. While the mechanical properties of actin in other states, especially the cross-linked gel state [68, 64] and the single filament itself [23], have been of a great interest, no measurement has been done on the mechanical property of an actin filament bundle cross-linked by actin bundling proteins.

In this paper we discuss the bending stiffness of a crystalline bundle of actin found in the acrosomal process of horseshoe crab sperm (see Fig. 3-1). During fertilization, the sperm cell of the horseshoe crab must penetrate the tough jelly coat of an egg.

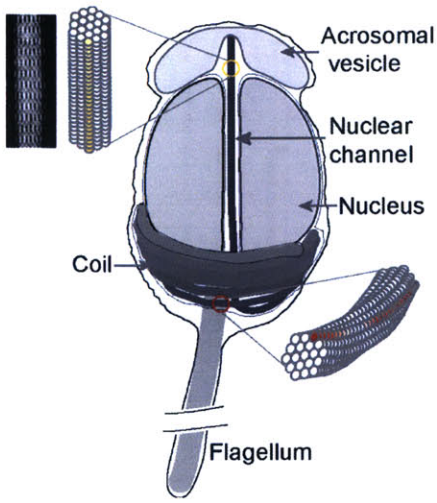


Figure 3-1: A schematic of unreacted *Limulus* sperm modified from electron micrographs, showing the proximal end of the acrosomal bundle lying in the nuclear channel while the rest of the bundle coiled around the base of nucleus. The blowups illustrate that the filaments are twisted in the coiled state, but straight in the true-discharge (TD) state.

This involves extension of the acrosomal process to bridge the sperm cell to the egg. Upon contact with the egg, the initially coiled bundle uncoils from the base of the nucleus and extends in average about five seconds from the head of the cell to form a 60 $\mu$m-long straight acrosomal process, called true discharge (TD) (see Fig. 3-1). Recent work has shown that the bundle consists of actin filaments cross-linked by scruin:calmodulin heterodimers [42]. To determine whether the acrosome bundle is mechanically suited for its function, we measure the bending stiffness using two independent methods. In the first method, a steady transverse flow is used to deflect the acrosomal bundle and the bending stiffness is derived from an analysis of the equilibrium shape. The second method employs a single pole magnetic trap to bend the bundle and relate the deflection to the applied magnetic force. Since the elastic modulus of a single actin filament is known [26], measuring the elastic modulus of the actin:scruin composite allows us to study the effect of cross-linking due to the bundling protein scruin.

## 3.2 Materials and Methods

### 3.2.1 Sample preparations

#### Sperm cells

Horseshoe crab (*Limulus polyphemus*) sperm (500 $\mu$l) is collected from healthy male and stored on ice. The collected sperm are washed at least twice in artificial seawater (ASW: 423mM NaCl, 9mM KCl, 9.27mM $CaCl_2$, 22.94mM $MgCl_2$, 25.5mM $MgSO_4$, 2.15mM $NaHCO_3$, 10mM Tris, pH adjusted to 7.9-8.0) by centrifugation at 750 g for 5 minutes, and resuspending in ASW to its original volume. Washed sperm are diluted 1:1000 in ASW. The experiments are conducted in a flat capillary flow-cell constructed with pieces of coverslip and double-sided adhesive spacers, sealed with inert vacuum grease (Apiezon Co., Manchester, UK) to prevent leaking.

#### Activation of the acrosome reaction

The flow-cell is first freshly coated with a tissue adhesive, BIOBOND (Cat 71304, EMS, Inc, Fort Washington, Pa), filled with diluted sperm, and incubated for about 10-20 minutes for secure adhesion to the surface of the coverslip. Saturated casein in ASW is diluted 100-fold with ASW, and several flow-cell volumes of the diluted solution are then added to the flow-cell to block the glass surface from non-specific binding of the extending acrosome and the beads used for flow visualization. After 20 minutes, the saturated casein solution is replaced with ASW containing 25mM $CaCl_2$. Calcium ionophore (A23187, 2mg/ml in ethanol) is diluted 1:10 with ASW containing 25 mM $CaCl_2$. Small amount (20 $\mu$l) of the diluted ionophore is injected into the flow cell to induce true discharge. Excess liquid is drawn from one side of the flow-cell as the diluted ionophore is pipetted into the other side.

#### Biotinylation of sperm cells

For the magnetic trap methods, streptavidin coated magnetic beads (Dynabeads M-280 streptavidin, Dynal Biotech, Inc. Cat 112.05) are attached to biotinylated sperm (see Fig. 3-2(a)). Sulfo-NHS-LC Biotin is stored at -20°C as a 10 mg/ml stock solution in anhydrous DMSO and diluted to 1:100 in ASWII. Sperm are washed

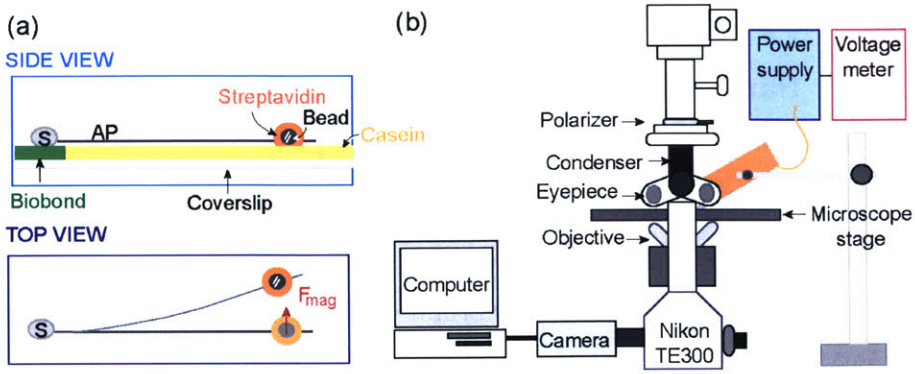


Figure 3-2: (a) A schematic representation of magnetic trap experimental set up. When the magnetic force is applied, the bead moves to bend the acrosomal bundle. By relating the shape of the deflected bundle with the applied force, one can deduce the bending stiffness of the bundle. (b) The magnet is situated close proximity to the top surface of the flow cell.

twice in ASWII (423mM NaCl, 9mM KCl, 9.27mM $CaCl_2$, 22.94mM $MgCl_2$, 25.5mM $MgSO_4$, 2.15mM $NaHCO_3$, 10mM Hepes, pH adjusted to 7.9-8.0). 10 $\mu$l of washed sperm (by centrifugation at 750 g for 1 minute twice) is added to 500 $\mu$l of prepared biotin solution. Sample is then incubated for 2 hours at room temperature on a rotating rack. Biotinylated sperm cells are then washed in regular ASW 3 times by centrifugation at 750 g.

### 3.2.2 Measurement setup

The extended acrosome can be bent within a plane either by a flow of the buffer or by a magnetic force. The bending stiffness can then be calculated from an analysis of the equilibrium shape and deflection of the acrosome.

#### Hydrodynamic measurement

After fixing the sperm to a glass coverslip using BIOBOND, the flow past the extended acrosomal bundle is induced inside the chamber by capillary absorption with a filter paper (54 Hardened 90mm Circles (Whatman, Inc., Clifton, NJ). Small polystyrene particles of diameter 0.175$\mu$m are used to visualize the flow. The cells and the particles are imaged under DIC-H optics at 100$\times$ magnification on a Nikon TE300 inverted

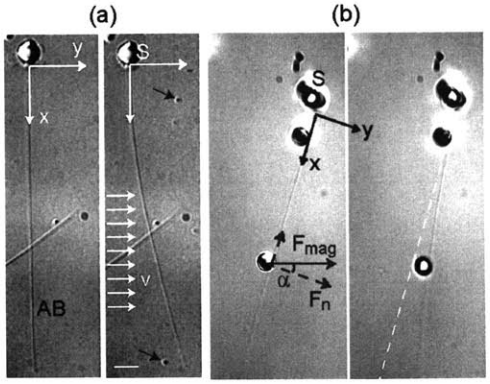


Figure 3-3: (a) A typical deflection of the acrosome under the distributed load by a steady flow is shown (before and after the flow). The arrows locate the particles used to measure the flow velocity. S indicates sperm head and AB indicates the average 60 $\mu$m acrosomal bundle. The scale bar on the right upper corner measures 5 $\mu$m. (b) DIC images of the reacted sperm before and after the voltage application (for this particular one: 10.8V). While keeping the position of the magnet at the same position, the velocities of the magnetic particles at different voltages are measured to determine the direction of the magnetic field and also to calculate the force using the Stokes formula. The direction of the field is almost horizontal (1-2° to horizontal line.) and thus is assumed to be perfectly horizontal. Normal component of the force (to long axis of the bundle) is calculated by taking cos$\alpha$.

microscope, and these images are captured with a Dage MTI (Model CD-300-RC, Dage-MTI, Inc., Michigan City, IN) video camera and recorded on a Sony SVO-9500MD S-VHS video cassette recorder. The velocity of flow is monitored using the trajectory of the particles travelling in the focal plane of the bundle. Selected video images are digitized at 30 fps using Apple Video player. In addition, the still images of the acrosome bundle in the absence and the presence of the steady flow are also captured to obtain the equilibrium shape (see Fig. 3-3(a)).

### Magnetic trap measurement

A focused load is applied to the bead-coupled bundle using a single pole magnetic trap. A 28mm diameter pole made of CMI-C steel is wrapped 550 times with a No. 24 gauge copper wire, turning the pole into an electromagnet. The magnetic pole is connected to a voltage supply (Kepco Power supply, Kepco, Inc., Flushing, NY) (see Fig. 3-2(b)). The sperm cell is affixed onto a coverslip and the acrosome reaction is

induced with the addition of ionophore into the flow-cell. Next, the magnetic beads suspended in ASW are introduced into the flow-cell, which is then rocked slowly back and forth to prevent the beads from fast sedimentation, giving enough time for the formation of a biotin-streptavidin bond between the sperm and the beads. We screen for the cells that have a single magnetic bead attached to the acrosome bundles. Once the static image of a bundle is stored, the voltage of the power supply is varied and the images of the deflected bundle at equilibrium are saved. We ensure that the bundle is only elastically deformed, by confirming that the bundle returns to its straight state when the magnetic trap is switched off (see Fig. 3-3(b)). For calibration of the magnetic force used to deflect the acrosome, we use a suspension of 2.8 $\mu$m magnetic beads in 4.95M $CaCl_2$ at a volume fraction ($\sim 10^{-7}$) at which magnetic and hydrodynamic interactions between beads can be neglected [1]. The same specified voltages used in the experiments are applied and the trajectories of the beads are recorded. The characteristic Reynolds number associated with the bead motion is of the order of $10^{-5}$, so that the magnetic force can be directly estimated from the viscous drag force using Stokes formula, $F_m = 6\pi\mu r_p v_m$, where $\mu$ is the viscosity of 4.95M $CaCl_2$ solution ($9.95\times10^{-3}$ Pa·s at 25°C), $r_p$ the particle radius, and the particle velocity (typically less than 9 $\mu$m/s). Since the force is sensitive to the position of the pole relative to the location of the beads, the location of the pole is not disturbed between the measurements and calibration.

### 3.2.3 Theoretical analysis

Here we outline the theoretical basis for the determination of the bending stiffness of the bundle from each of the experimental methods.

#### Hydrodynamic flow method

Electron micrographs of the acrosomal bundle reveal that the bundle is a non-prismatic rod of hexagonally packed and cross-linked actin filaments with a continuously increasing radius from the tip to the base (15-80 filaments). For analysis, we assume the bundle to be a linearly tapering rod of length $L$ and of radius $r(x)$. When a tapered

elastic rod of stiffness *EI(x)* is subject to a force per unit length *f*, its shape *y(x)* for small deflection is determined by the solution of the differential equation

$$\frac{d^2}{dx^2}(EI(x)\frac{d^2y}{dx^2}) = f. \tag{3.1}$$

In the presence of a steady flow, the Stokes drag per unit length for a long slender rod moving near a single plane wall is [22]

$$f = 2\pi\mu v/\cosh^{-1}(h/R_{ave}). \tag{3.2}$$

Here, $\mu$ is the viscosity of the medium, $v$ the velocity of the flow, $h$ the distance between the bundle and the wall, and $R_{ave}$the average radius of the bundle. The bundle is assumed to be clamped at the proximal end consistent with observations, while the distal end is free of forces and moments. Therefore, the boundary conditions supplementing these are [22].

$$y = 0,\ \frac{dy}{dx} = 0 \ \texttt{at x=0;} \qquad \frac{d^2y}{dx^2} = 0,\ \frac{d^3y}{dx^3} = 0 \ \texttt{at x=L} \tag{3.3}$$

One way to obtain the Young's modulus $E$ using Eq. 3-1 is to find a polynomial fit to the experimental deflection curve and express $E$ as a function of $f$ and $I(x) = \pi/[4(R_{min}+x\tan\beta)^4]$ where $R_{min}$ is the radius of the distal end and $\beta$ the taper angle. Unfortunately, this approach leads to large errors due to the sensitivity of the high order polynomial fit to the experimental data and does not yield a reliable estimate of $E$.

To circumvent this difficulty, we model the bundle as a tapering segmented rod made of n-cylinders whose radii, $r_n$, vary according to the linear function fitted to the slope of the bundle obtained from electron micrographs (see Fig. 3-4). The tapering angle and $R_{min}$ are estimated by taking the average of the tip radii obtained from cross sectional electron micrographs of 13 different cells. The slope of the bundle is expressed as $S = (R_{max} - R_{min})/L_{tot}$ , where $L_{tot}$ is the average total bundle length, 60 $\mu$m. The radius is $r_n(x_n) = R_{base} + S(L/N - x_n)$ with $R_{base}$ being the radius of the bundle at the junction (the clamped boundary) and $x_n = Ln/N$ is the location of the end of each segment. Since the acrosome bundle does not always extend to its full

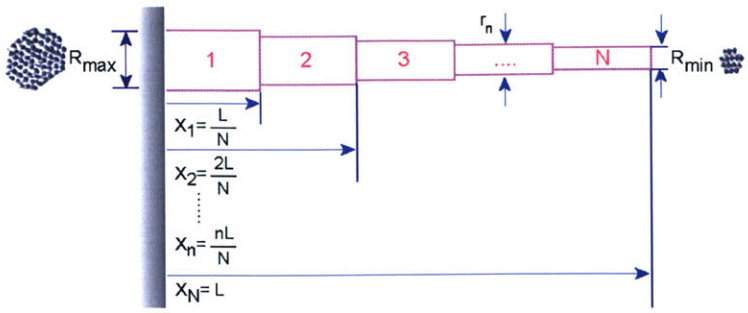


Figure 3-4: The acrosomal bundle of horseshoe crab is modelled as a linearly tapering elastic rod made of n-cylinders. From electron micrographs of cross-sectional sperm cells, the maximum and minimum radii ($R_{max} \sim 68$nm and $R_{min} \sim 24$nm) are measured and the slope $S$ of the taper is calculated to be $7.3\times10^{-4}$. The radii $r_n$ of each segment vary according to the linear function fitted to the slope of the bundle such that $r_n(x_n) = R_{base} + S(L/N - x_n)$. At two ends of the drawing, the EM images of the negatively stained acrosomal bundle are shown.

length with its extended length varying from cell to cell (45$\sim$ 65 $\mu$m), $R_{base}$ depends on the length of the extended bundle, with $R_{base} = R_{min} + L(R_{max} - R_{min})/L_{tot}$ (see Fig. 3-4).

We assume each segment in the bundle to obey linear elastic theory, and apply the method of superposition to obtain the total deflection at the tip of the entire bundle. This method is valid when the material is linear, elastic, and isotropic, and if the deflection and taper are small. As an illustration, consider a cantilever beam (see Fig. 3-5) under a distributed load $f$. The tip deflection $\delta_{tot} = \delta_B + \delta_o + \theta_c(L/2)$ where $\delta_B$ is the deflection of the $\overline{AB}$, $\delta_o$ the deflection of the $\overline{OA}$, and $\theta_c(L/2)$the transverse displacement due to the rigid body rotation $\theta_o$ of the boundary $A$. Using the same superposition principle for a tapering rod made of N-cylinders yields the following

$$\delta_n = \frac{f}{8EI_n}(\frac{L}{N})^4 + \frac{M_n}{2EI_n}(\frac{L}{N})^2 + \frac{V_n}{3EI_n}(\frac{L}{N})^3 + (\frac{f}{6EI_n}(\frac{L}{N})^3 + \frac{M_n}{EI_n}(\frac{L}{N}) + \frac{V_n}{2EI_n}(\frac{L}{N})^2)(L - \frac{L}{N}n),$$

$$n = 1 : N-1;$$

$$\delta_N = \frac{f}{8EI_n}(\frac{L}{N})^4, \quad n = N \tag{3.4}$$

where $M_n = f(L^2 - x_{n2})/2 + fLx_n$ is the moment at the end of n$^{th}$ segment ($x_n = (L/N)n$), $V_n = fL - fx_n$ the shear force at the end of n$^{th}$ segment, and $I_n = \pi/(4{r_n}^4)$

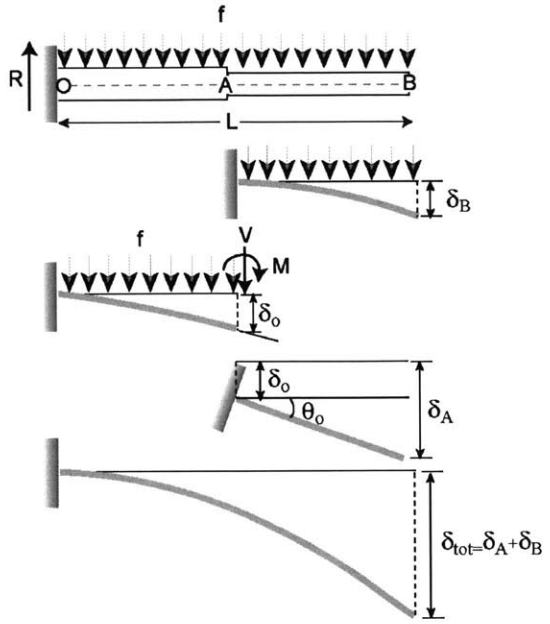


Figure 3-5: Cantilever beam with two different moments of inertia due to the differences in their cross-sectional areas is illustrated with the elements contributing to the total deflection $\delta_{tot} = \delta_A + \delta_B = \delta_B + \delta_o + \theta_o(L/2)$.

the moment of inertia for the n$^{th}$ segment. The total deflection is then

$$\delta_{tot} = \delta_1 + \delta_2 + \delta_3 + \ldots \delta_N \tag{3.5}$$

Eq. (5) yields the Young's modulus $E$ given the experimentally measured values of $\delta_{tot}$, $L$, and $r_n$,

### Magnetic trap method

In the case of magnetic trap measurements, a similar analysis can be performed with a point load $F_m = f \cdot \delta(x - L)$, where is the usual Dirac-delta function. Integrating Eq. 3-1 then leads to

$$\frac{d}{dx}(EI(x)\frac{d^2y}{dx^2}) = F_m. \tag{3.6}$$

As in the previous case, we use the principle of superposition for a bundle composed of n-cylinders ($1 \leq n \leq N$) to determine the total deflection $\delta_{tot} = \delta_1 + \delta_2 + \delta_3 + \ldots \delta_N$,

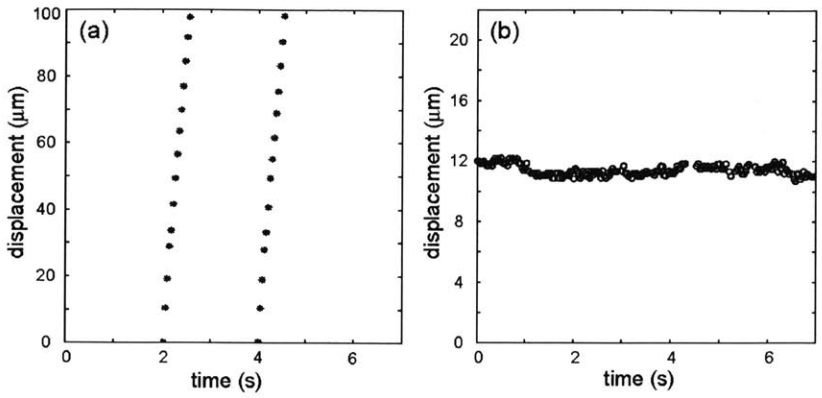


Figure 3-6: (a) Trajectories of the particles are used to obtain the flow velocity. At least two particles lying in the plane of focus at different locations are chosen in the field of view to ensure the uniform flow within the field; the constant particle velocities indicate that the flow has reached its equilibrium state. (b) The bundle undergoes thermal motion about its average position at equilibrium. To minimize the uncertainty in the measurement, the average value is calculated from data points taken at its equilibrium for 5-10 seconds. Flow is then stopped to ensure that the bundle relaxes back to its original straight configuration.

and thence $E$. When the distributed hydrodynamic load is replace by a point load due to the magnetic bead, we find

$$\delta_n = \frac{M_n}{2EI_n}(\frac{a}{N})^2 + \frac{V_n}{3EI_n}(\frac{a}{N})^3 + (\frac{M_n}{EI_n}(\frac{a}{N}) + \frac{V_n}{2EI_n}(\frac{a}{N})^2)(a - \frac{a}{N}n),$$
$$n = 1 : N-1;$$
$$\delta_N = \frac{F_\perp}{3EI_n}(\frac{a}{N})^3, \quad n = N \tag{3.7}$$

where $M_n = F_\perp(a - x_n)$ and $V_n = F_\perp$. Using Eq. 3-7, we can then determine $E$ given the experimentally measured values of $F_\perp$, $\delta_{tot}$, $a$, and $r_{ave}$.

## 3.3 Results and discussions

### 3.3.1 Hydrodynamic flow method

Particle tracking is used to measure the flow velocity and confirm that it is steady. At least two particles lying in the plane of focus are chosen within a field of view to ensure that a uniform flow field exists (see Fig. 3-6(a)). From Eq. 3-2, the force density

applied to the deflecting bundle is calculated using $\mu$=$10^{-3}$ Pa· s, $h\sim$ 1 $\mu$m, $R_{ave}$ =46nm, and $v$ typically 45-120 $\mu$m/s. The measured tip deflection ranges between 2.9-11.5 $\mu$m, validating the small deflection assumption used in deriving Eq. 3-1. As shown in Fig. 3-6(b), the tip undergoes fluctuations about its average position at equilibrium. To minimize the uncertainty in the measurement, the displacement of the tip is averaged over 5-10 seconds.

Fig. 3-3(a) shows a typical deflection of the acrosome under the distributed load by a steady flow. The Young's modulus, $E_{taper}$, is obtained from Eq. 3-4 and 3-5 using the previously defined parameters and its value is found to be $E_{taper}$=2.5±0.72 GPa. Since $I$, the moment of inertia, scales as the fourth power of $r$, $EI$ rises from $0.9\times10^{-21}$Nm$^2$ to $16\times10^{-21}$Nm$^2$ for the estimated constant value of $E_{taper}$. The average bending stiffness of $\sim 5\times10^{-21}$Nm$^2$ corresponds to an average persistence length of $L_p = EI/k_BT\sim$1.2 m, implying that the acrosome bundle is clearly impervious to thermal fluctuations over cellular dimensions. For comparison, we find that approximating the rod as a cylinder with a constant radius, $R_{ave}$, leads to $E_{ave}$=2.38±0.81GPa using $E_{ave} = fL^4/(2\pi R_{ave}^4\delta_{tot})$. Although the numerical value $E_{ave}$ is not very different from $E_{taper}$, the tapering rod model leads to a shape that is much closer to the experimentally observed one (see Fig. 3-7(a)).

### 3.3.2 Magnetic trap method

The single pole magnetic trap experiment provides us with an independent measurement of the bending stiffness. We calibrate the force following the analysis by Amblard et al. by relating the magnetic field to the hydrodynamic forces on the beads suspended in a solution of 4.95M $CaCl_2$ [1]. Velocities are measured for beads located at least 30$\mu$m from the bottom of the flow cell to guarantee that wall effects are negligible and their values are tabulated in Table 1.

We first use Stokes formula, $F_m = 6\pi\mu r_p v_m$, to obtain the magnitude of the force. The perpendicular component of the force is $F_\perp = F_m \cos\alpha$ where $\alpha$ is the angle between the direction of the moving bead and the bundle axis (Fig. 3-3(b)). With the values of $F_\perp$, $\delta_{tot}$, and $a$, the mean elastic modulus is found to be

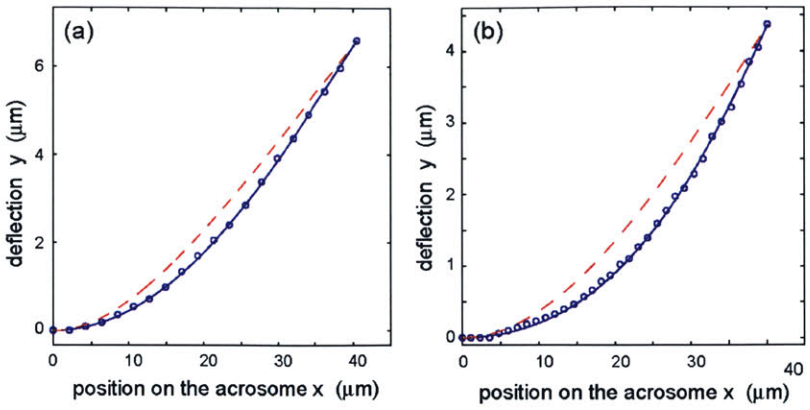


Figure 3-7: (a) Experimentally obtained shape of the deflected acrosomal bundle in steady hydrodynamic flow (open circle) is shown along with two analytical curves. The solid line represents the theoretical curve using the tapered rod model while the dashed line represents the curve obtained by $y(x) = f(x^4 - 4x^3L + 6x^2L^2)/6\pi E_{ave}R_{ave}^4$ with the average value of $E_{ave}$ assuming a uniform thickness rod. We define a goodness of the theoretical fit to the experimental data as $\psi^2 = 1 - \frac{1}{N}\sum(\frac{y(x_i)-t(x_i)}{y(x_i)})^2$ where $y(x_i)$ is the experimental data, $t(x_i)$ the theoretically predicted value, and $N$ the number of data along the curve, leading to $\psi^2_{taper}$=0.9984 and $\psi^2_{uniform}$=0.8978, with $\psi^2$=1 corresponding to a perfect fit. For this particular data, $E_{taper}$ = 2.2 GPa, $E_{ave}$ = 2.3 GPa, and the $EI_{ave}$ =8×10$^{-21}$Nm$^2$. The distributed load density $f$=2.4×10$^{-7}$ N/m. (b) Experimental shape of the deflected acrosomal bundle with the point load, $F_m$, exerted by the magnetic field (open circles), along with two analytical curves. The solid line represents the theoretical curve using the tapered rod model while the dashed line represents the theoretical curve for uniform thickness rod by $y(x) = 2F_mx^2(3a - x)/3\pi ER_{ave}^4$. For this particular data, E$_{taper}$ =1.4 GPa, E$_{ave}$=1.2 GPa, and the $EI_{ave}$= 4.1×10$^{-21}$Nm$^2$. The theoretical curve from the tapered model fits the experimental deflection well with $\psi^2_{taper}$=0.9967 while the uniform rod model shows a large discrepancy with $\psi^2_{uniform}$=0.8228.

E$_{taper}$=1.34±0.34GPa, while the bending stiffness $EI$ varies from 0.37×10$^{-21}$Nm$^2$ to 10.6×10$^{-21}$ Nm$^2$ from the tip to the base (Table 1). Fig. 3-7(b) shows the theoretical fit to experimentally obtained deflection.

A few potential sources for variation in the obtained results should be considered. First and most important, there are variations among individual sperm cells. A second likely source of variations lie in the inaccuracy associated with particle velocity measurements due to a finite optical depth-of-field, which can give rise to ~2 folds variations in the flow velocity estimates. In addition, there could be an error associated with the estimate of the bundle taper.

Table 3.1: Young's modulus ($E$) measurements at various voltages in magnetic trap method: To calibrate the forces at specified voltages, the velocities of 2.8 $\mu$m diameter magnetic beads moving in 4.95M $CaCl_2$ solutions are measured. Since the maximum velocity ($V$) of the beads at the highest voltage does not exceed 9 $\mu$m/s, leading to the Reynolds number of the order of $10^{-5}$, the magnetic force ($F$) can be directly estimated from the drag force using the Stokes formula,$F_m = 6\pi\mu r_p v$, where $\mu$is the viscosity of 4.95M $CaCl_2$ solution, $\mu$=9.95$\times 10^{-3}$ Pa·s, $r_p$ the particle radius, and $v$the particle velocity. The $E$ values corresponding to each voltage are calculated from Eq. 3-7.

| Voltage | 5V | 10V | 15V | 20V | 25V |
|---|---|---|---|---|---|
| V($\mu$m/s) | 1.3±0.2 | 2.1±0.1 | 3.5±0.2 | 4.8±0.6 | 8.9±0.4 |
| F(pN) | 0.35±0.05 | 0.56±0.07 | 0.91±0.05 | 1.25±0.16 | 2.4±0.02 |
| E(GPa) | 1.26±0.62 | 1.18±0.2 | 1.3±0.15 | 1.58±0.11 | 1.46±0.1 |

We now consider the relation of the stiffness of the bundle to the stiffness of a single actin filament. Each bundle of acrosome consists of 15-80 filaments arranged along a tapering cross-section. If the acrosome bundle is assumed to be a rod of a uniform radius, $R_b \sim$ 46nm, made of 50 actin filaments cross-linked by scruin, the average stiffness $EI_{ave} \sim 8\times 10^{-21}$ Nm$^2$ corresponds to a material with Young's modulus of 2.4GPa ($EI_{bundle} = E\pi R_b^4/4$). This value for Young's modulus is comparable with that of a stiff elastomer and similar to that of pure actin filaments ($\sim$ 2.6GPa)[64]. In contrast, if we suppose that we have a bundle of 50 uncross-linked actin filaments of radius $r_f$ in a rope-like configuration, the stiffness of such a bundle $EI_{rope} = (E\pi {r_f}^4/4)n \sim 2.6\times 10^{-23} Nm^2$. Therefore, the cross-linked acrosome actin bundle is more than 300 times stiffer than a ropy bundle of uncross-linked actin filaments of a similar radius. Thus the bundle bending stiffness is determined by the elasticity of actin since the elastic modulus of scruin is much larger than that of actin. Electron micrographs lend some credence to our hypothesis; they show that there is a high density of scruin cross-links [47], which allows for the substantial stiffening seen experimentally. Here, the functional requirement for the actin bundle to penetrate the tough coat of the egg is well met by the stiffening induced by the tight cross-linker scruin. In contrast, a bundle of actin that is cross-linked by a weaker cross-linker such as $\alpha$-actinin will be much softer.

# Chapter 4

# Force of an actin spring

## 4.1 Introduction

The acrosome reaction of the horseshoe crab, *Limulus*, sperm is an unusual example of actin-based motility. *In vivo*, upon contact with the egg jelly coat, a bundle of actin filaments cross-linked by scruin:calmodulin heterodimers extends from the head of the sperm through a nuclear channel to form a 60 $\mu$m-long finger of membrane, the acrosomal process (see Fig. 4-1). Based on structural analysis of the actin bundle before and after activation, DeRosier and Tilney suggested a spring-based mechanism in which elastic strain energy stored in the conformation of the coiled bundle is converted to mechanical work. Our study has shown that the uncoiling of the bundle proceeds like a zipper wherein a small region of the coiled bundle untwists and this conformational change then propagates along the bundle with continuous binding of $Ca^{2+}$. This localized uncoiling gives rise to an incremental energy release during the reaction, corresponding to a constant force generation during the reaction.

In this study, we measure the force generated during the acrosomal reaction in the horseshoe crab sperm using two independent methods. In the first method, we embed sperm cells in a solid block of agarose and trigger to induce the extension of the acrosome bundle. The acrosome extends against a shear drag exerted by the agarose and the reaction stalls when the opposing force exceeds the force produced by the acrosome. We find that at the concentrations higher than 1.5 % (w/v), the extending acrosome stalls and the stall length becomes shorter with increasing agarose

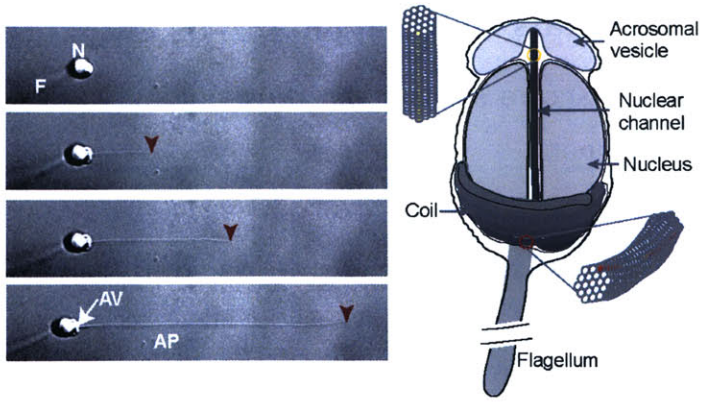


Figure 4-1: The acrosomal reaction in *Limulus* sperm: (a) Upon activation by the presence of an egg or $Ca^{2+}$, a 60 $\mu$m long acrosomal bundle extends out of a 5 $\mu$m sperm cell in average five seconds when activated in ASW. N: nucleus, F: flagellum, AV: acrosomal vesicle, and AP: acrosomal process. (b) A schematic of un-reacted sperm modified from electron micrographs, showing the proximal end of the acrosomal bundle lying in the nuclear channel while the rest of the bundle is coiled around the base of nucleus. The blowups illustrate that the filaments are twisted in the coiled state, but straight in the true-discharge (TD) state.

concentrations. Stall force is calculated from the measured values of stall length and the stresses estimated from the macroscopic penetration test. Secondly, we use methylcellulose (MC) as a viscoelastic thickening agent to mechanically slow down the extension rate of the acrosome. We employ both macro-rheology and multi-particle tracking (MPT) micro-rheology techniques to characterize the viscosity of the MC solutions to estimate the force. This method yields the lower bound estimate of the acrosome force and validates that our measured stall force is in a reasonable range. For both methods, we employ a novel way to trigger the acrosomal reaction using 488nm laser irradiation. Based on the estimated force values, we also confirm that the acrosomal reaction produces sufficient force to meet its functional role of penetrating the egg.

## 4.2 Materials and Methods

### 4.2.1 Microscope sample preparations

#### Reaction medium

For the agarose experiments, 0.5 % (w/v), 1.0 %, 1.5 %, 2.0 %, 2.5 %, and 3 % agarose gels are prepared by mixing low-melt-agarose powder (gel point: 29°C) in ASW. The mixtures are boiled with agitation until the solutions become completely clear. The gel is cooled to solidify at room temperature (25°C); the solidified agarose gels turn opaque. The agarose solution exhibits a hysteresis between its melting point (>50 °C) and gel point (29°C), so it is incubated at 65-70°C for 5-10 minutes to re-melt and saved in small aliquot for future uses. For methylcellulose (MC) experiments, we prepare 1.0 % (w/v), 2 %, 2.5 %, 3.5 %, 4 %, 5 %, and 6 % MC solutions dissolving MC powder in heated ASW (Sigma, M0387: MW of 63,000 Da). Homogeneity of the solution largely depends on the preparation method and we follow the protocol suggested by the manufacturer. Briefly, ASW is heated until it starts to boil and the MC powder is added to the hot ASW with gentle agitation. The mixture is agitated in warm water-bath for about 1 hour, and cooled to room temperature with continuous agitation until the particles are thoroughly wetted and evenly dispersed. The opaque particulate mixture is then cooled with gentle stirring in a cold room (4°C) overnight. The dispersion becomes translucent and the viscosity increases when the MC becomes water-soluble. The solution is spun at 3000 g for >1 hr to remove bubbles.

#### Sperm cells

Horseshoe crab (*Limulus* polyphemus) sperm (500 $\mu$l) is collected from healthy male and stored on ice. The collected sperm are washed at least twice in ASW by centrifugation at 750 g for 5 minutes. For the agarose experiment, a small aliquot of agarose is re-melt at 65-70 °C water-bath for a couple of minutes and the melt agarose is cooled to about 31-33°C before the pelleted sperm cells are added to its final volumetric ratio of 1:500 (cells: agarose). The sample is mixed well by vortexing it for about 10 seconds and injected into a pre-warmed flow chamber (22mm×10mm×0.2mm) con-

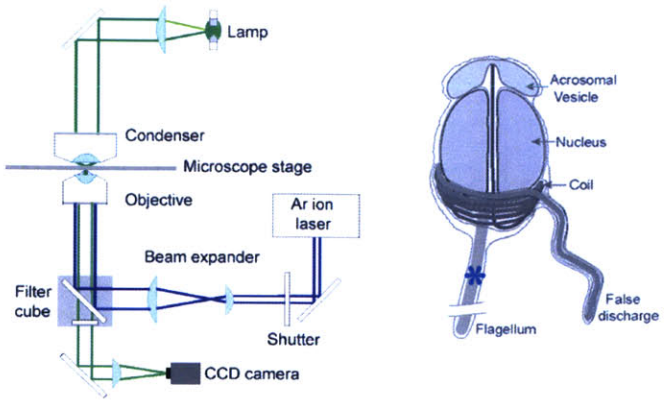


Figure 4-2: We use a novel way of inducing the acrosomal reaction by irradiating a focus laser of 488nm on the flagellum (courtesy of Ricardo Brau, Mathew Lang Lab, MIT.)

structed with pieces of coverslip and double-sided adhesive spacers. The agarose filled flow chamber is cooled quickly at 4°C for 10mins and stored at room temperature before use. The low-melting-point (LMP) agarose gel is ideally suited for our experiments as sperm cells are viable up to $\sim$ 40°C. Alternatively, washed sperm cells are diluted 1:2000 in ASW, injected into a flow chamber that is pre-treated with a tissue adhesive, BIOBOND (Cat 71304, EMS, Inc, Fort Washington, PA), and incubated for 10-20 minutes for cells to securely adhere to the bottom of the flow chamber. The chamber is pre-warmed to $\sim$ 30°C on a heating block and the cooled melt agarose (31-33°C) is injected into the flow cell to completely replace ASW. The agarose filled flow chamber is rapidly cooled again at 4 °C the same way. The latter method is also used for the MC experiments except that the chamber needs not to be pre-warmed.

### Activation of the acrosomal reaction

We employ a novel way of inducing the acrosomal reaction using 488nm laser irradiation (see Fig. 4-2). Typically, the acrosomal reaction in the *Limulus* sperm as well as in other marine invertebrates is induced by the use of calcium ionophore to bring the extra-cellular calcium into the cytoplasm. Our recent finding has shown that a focused 488nm laser of its output power >7mW is able to trigger the acrosomal reaction when irradiated on certain parts of the sperm. The laser irradiation technique

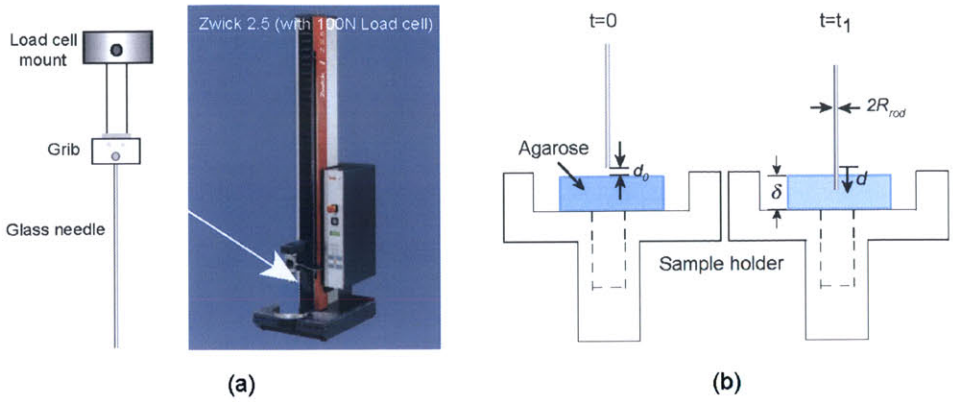


Figure 4-3: Experimental setup to perform a shear test on the agarose gel. (a) We use the Zwick series 2.5 with a 100N load cell with a sensitivity of 0.001N. This instrument is operated in a compression test mode with a displacement control to move the probe at a specified constant velocity. (b) A specimen holder has a through hole in the middle so that the probe can puncture through the slab of agarose gel.

enables us to trigger the reaction on demand.

### 4.2.2 Characterization of the materials

#### Agarose

We use the Zwick 2.5kN instrument to perform a penetrating test to characterize the shear stress the agarose is exerting on the extending acrosome (See Fig. 4-3(a)). We operate the instrument in a compression test mode and we move the probe at a fixed velocity in a displacement control mode. Agarose is a porous solid whose pore sizes are of the order of 100-500nm, comparable to that of the acrosome tip diameter. Therefore, it is natural to assume the bundle to travel both through the void space and through the solid and the interactions between the bundle and the medium is not simple. To characterize such interactions, it is desired to use a probe of similar diameter as the acrosome, yet the following experimental difficulties arise: 1) the sensitivity of the currently available load cell is only $\sim$ 0.001N, 2) manufacturing a rod of 100nm diameter is very difficult, and 3) handling of sub-micron scale needles is extremely challenging.

In this study, we assume the gel to be homogeneous continuous medium as a first

Figure 4-4: Phase contrast image of a stainless steel needle with $R_{Rod} = 0.54$ mm with a tapering tip. The needle becomes a uniform thickness beyond 6mm from the tip. The smallest gradation in the ruler is 0.1mm.

approximation. For such an ideal solid, the shear stress along the probe should be independent of the probe diameter and the frictional force that resists the motion of the probe should simply scale with the diameter of the probe. Furthermore, the stress should not be a function of the travelling velocity of the probe. First, we choose a stainless steel probe of $R_{Rod} = 0.54$ mm with a tapering tip (see Fig. 4-4), and set the probe velocity to be 1.0 mm/s such that a normalized velocity $\tilde{V} = V/R_{Rod} \sim 2$ $s^{-1}$, corresponding to the acrosomal reaction rate of 0.04$\mu$m/s for the bundle of 48nm tip diameter. As shown in Fig. 4-3(b), the probe is setup to penetrate into a slab of agarose (thickness $\delta$) and puncture through. During the penetration process inside the sample (transient state), the force exerted by the load cell should be balance by two force components. First one involves the opening of the crack in front of the extending tip and the second component is the frictional force along the surface of the probe that resists the motion such that $F_{tot} = F_{Crack} + F_{Drag}$. Once the rod punctures through the slab (steady state), there remains only the frictional force since there is no more agarose front to open. By comparing the force values at the transient and steady states, we can deduce the contribution of force required to open a new front inside the agarose gel. We repeat the experiments varying the diameter of the probes and the probe velocity to investigate the effects of these parameters in the stress measurements.

### Methylcellulose

We used MC solution to mechanically slow down the acorosomal reaction. To characterize the viscoelastic properties of the MC solution that work against the extending acrosome, we employ both the macro- and micro-rheology.

**Macrorheology** The mechanical response of the viscoelastic MC solutions is measured with a rheometer (AR2000, TA Instruments) using the 40 mm titanium cone-plate geometry with its gap distance of 50 $\mu$m. We first probe the elastic response as a function of strain, $\gamma$ in a linear oscillatory mode at a fixed frequency $\omega$ =1 rad/s to determine the range of the linear elastic regime. In the linear elastic regime with the measured strain, $\gamma$, typically <0.1, we measure the frequency dependent elastic modulus, $G'(\omega)$, and loss modulus, $G''(\omega)$ in the frequency range of typically $\omega$ =0.08 - 300 rad/s. Additionally, we probe the viscosity as a function of strain rate, $\dot{\gamma}$ in a steady flow measurement. To test the applicability of the Cox-Merz rule, the shear viscosity as a function of shear rate, $\eta(\dot{\gamma})$ measured from steady flow measurement is compared with the complex viscosity as a function of angular frequency, $\eta^* = (G'^2 + G''^2)^{1/2}/\omega$.

**Microrheology** The tip of the acrosome is only $\sim$ 50nm in its diameter and thus it is likely that the local environment the tip encounters may be entirely different. In order to probe the local properties the tip of the acrosome explores, tracer particles of a 100nm in diameter are added in the MC solutions and mixed gently with a pipette tip. We use PEG (polyethylene glycol) coated particles to prevent particle aggregation. The MC-particle mixture is injected in a glass sample chamber and sealed with high-vacuum grease to prevent evaporation and drifting during the measurement. We image in average 30-50 rhodamine labelled particles per field using fluorescence microscopy with 100$\times$ objective with a numerical aperture (N.A.) of 1.2. Their dynamic motions are recorded at 18.5 frames per second using a Hamamatsu digital camera. Several thousand frames are captured, ensuring good statistical accuracy for time scales up to hundreds times the frame rate. The particle centers are detected in each frame to an accuracy, $\delta$, of 20 nm and the time evolution of each particle position is determined. To explore the wall effects, we image at various distances away from the surface into the sample. We filter for the particles that remain in the field of view for at least 90s and we calculate the individual particle mean-squared displacement (MSD)$\langle \Delta x^2(\tau) \rangle$ as a function of time. In general, the ensemble-averaged MSD can be related to the frequency-dependent linear moduli using a generalized Stokes-Einstein

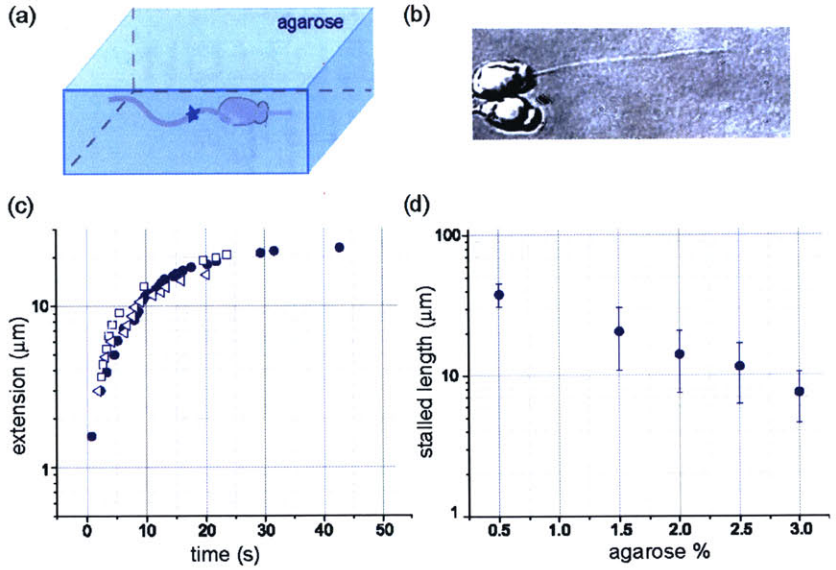


Figure 4-5: (a) DIC image of a stalled acrosome at 1.5 % agarose gel: scale bar measures 5 $\mu$m (b) As the bundle becomes longer, the shear drag along the bundle grows larger, slowing down the extension velocity until it finally stalls when the sum of $F_{Drag} + F_{Crack}$ wins over the acrosomal force. (c) Stall lengths of the acrosome become shorter with increasing concentration of agarose as the frictional drag becomes larger.

relation: $\tilde{x}^2(s) = k_B T/\tilde{G}(s)$, where $\tilde{x}^2(s)$ is the Laplace transform of $\langle \Delta x^2(\tau) \rangle$ and $\tilde{G}(s)$ is the viscoelastic response as a function of the Laplace frequency $s$. To compare with bulk rheology measurements, $\tilde{G}(s)$ is transformed into the Fourier domain to obtain $G^*(\omega)$, which is the complex shear modulus, the sum of real and imaginary components: $G^*(\omega) = G'(\omega) + iG''(\omega)$. From this complex shear modulus, we estimate the complex viscosity as a function of angular frequency, $\eta^*(\omega) = G^*(\omega)/\omega$ to obtain the local viscosity the acrosome experience as it extends in the MC medium.

## 4.3 Results and discussions

### 4.3.1 Agarose

When we irradiate laser of >7mW on the flagellum of *Limulus* sperm, the acrosomal reaction is triggered and the acrosomal bundle extends out of the sperm cell following

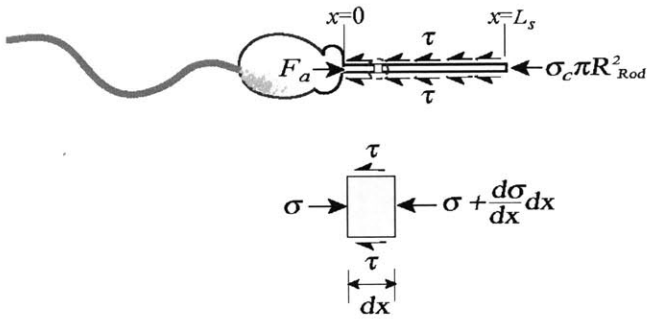


Figure 4-6: Forces acting on the extending acrosome. When the embedded cells react, the extending acrosomal bundle inside the agarose is opposed by both the frictional force, $F_{Drag}$, along the bundle and the crack opening force $F_{Crack}$ at the tip. We balance forces on a differential element in the bundle at the moment it stalls $x$=$L_s$ to estimate $F_a$.

the rupturing of the vesicle (see Fig. 4-1). Typically, the acrosomal bundle extends $\sim$ 55-60 $\mu$m at a constant velocity of $\sim$ 12 $\mu$m/s. When the embedded cells react, the extending acrosomal bundle inside the agarose is opposed by both the frictional force, $F_{Drag}$, along the bundle and the crack opening force $F_{Crack}$ at the tip. As the bundle becomes longer, the shear drag along the bundle grows larger, slowing down the extension velocity until it finally stalls when the sum of $F_{Drag} + F_{Crack}$ wins over the acrosomal force (see Fig. 4-5(b)). Furthermore, the stall lengths of the acrosome become shorter with increasing concentration of agarose as shown in Fig. 4-5(c). At 0.5 %, 1.5 %, 2.0 %, 2.5 %, and 3.0 %, the average stalled lengths are 37.9$\pm$7.0 $\mu$m, 20.6$\pm$9.8 $\mu$m, 14.2$\pm$6.1 $\mu$m, 11.6$\pm$5.3 $\mu$m, and 7.6$\pm$3 $\mu$m, respectively.

As illustrated in Fig. 4-6, we balance forces on a differential element in the bundle at the moment it stalls $x$=$L_s$.

$$\sigma\pi R_a^2 - (dx\frac{d\sigma}{dx} + \sigma)\pi R_a^2 - 2_a = 0 \tag{4.1}$$

Using the boundary conditions that $\sigma(x = 0) = F_a/\pi R_a^2$ and $\sigma(x = L_s) = \sigma_c$, we obtain the expression for the acrosome stalling force $F_a$ as

$$F_a = F_{Crack} + F_{Drag} = \sigma_c\pi R_a^2 + \tau 2\pi R_c L_s \tag{4.2}$$

where $R_a$ is the acrosomal bundle radius and $\sigma_c$ the crack opening stress. We provide estimates of the stress values, $\tau$ and $\sigma_c$, associated with friction along the bundle and

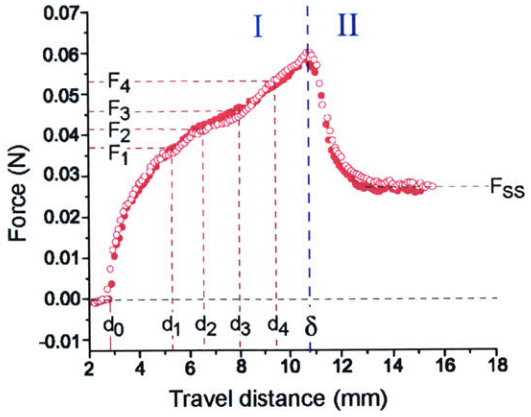


Figure 4-7: Force vs. travel distance of the probe ($R_{Rod}$=0.54mm) as it penetrates through a slab of 3 % agarose. The probe makes an initial contact with the gel when $d = d_o$ and punctures through when $d = \delta$. In the transient region I, both frictional drag and crack opening force resist the penetrating probe while only frictional drag exists in the steady state regime II.

crack opening at the tip from the penetration test results. As a first approximation, we assume the agarose to be a continuous and homogeneous solid block and measure the shear stress and crack opening stress using a macroscopic probe of $R_{Rod}$=0.54mm.

As shown in Fig. 4-7, we can divide the force-displacement curve into two distinct regimes, (I) transient and (II) steady state regime. In the transient regime I, both frictional drag and crack opening force resist the penetrating probe while only frictional drag exists in the steady state regime II. From the steady state force, $F_{ss}$, we first calculate the steady state shear stress which is purely due to the frictional drag along the bundle, $\tau_{ss} = F_{ss}/2\pi R_{Rod}\delta$, where $\delta$ is the total thickness of the agarose block. The contribution from the crack opening is then calculated by subtracting the frictional drag force from the total force, $F_1$, $F_2$, $F_3$, $\cdots$, $F_n$, in the transient regime (I).

$$F_{Crack} = F_n - F_{Drag} = F_n - \tau_{ss} 2_{Rod}(d_n - d_o) \tag{4.3}$$

From the obtained value of crack opening force, we calculate the stress associated with opening the crack at the tip as $\sigma_c = F_{Crack}/\pi R_{Tip}^2$. Assuming an ideal continuum solid material where $\sigma_c$ is conserved, we estimate the force required for the acrosomal bundle to open up the crack by simply multiplying the stress $\sigma_c$ by the tip area,

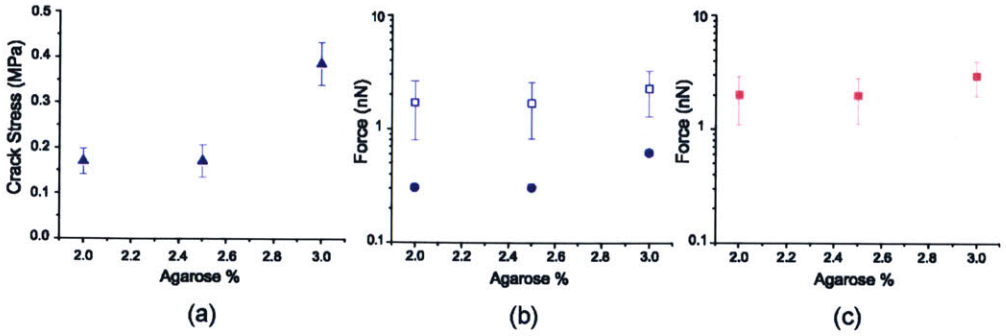


Figure 4-8: Shear test results for the stainless steel needle of $R_{Rod}$=0.54mm (a) Crack stress obtained from the transient regime increases with increasing agarose concentration. (b) Forces vs. agarose concentrations: Open squares are drag force obtained from steady state regime and solid circles represent the crack forces calculated by multiplying the measured crack stress by the cross-sectional area of the tip. (c) Total acrosomal force at the moment of stalling is found by $F_a = F_{Crack} + F_{Drag}$. We have a consistent value of total stalling force $F_{Stall}$ for all concentrations of agarose whose average is $\sim$ 2.3nN.

$F_{Crack(a)} = \sigma_c \pi R^2_{Tip(a)}$.

As shown in Fig. 4-8(a), the steady state shear stress $\tau_{ss}$ increases with the increasing concentration of agarose and $\sigma_c$ does not change much from 2 % to 2.5 % but increases by more than a factor of 2 for 3 %. Since both stresses increase with increasing concentration of agarose, it is expected that we observe the stall length of the acrosome become shorter with increasing concentrations of agarose (see Fig. 4-5(b)). Given the estimates of $\tau_{ss} = \tau$, $\sigma_c$ and the measured values of $L_s$ at various agarose concentrations, we obtain the acrosome force at the moment of stalling using Equation (4-1). Fig. 4-8(b) shows the relative magnitude of the drag force and crack opening force measured with a stainless steel probe of $R_{Rod}$= 0.54mm at its probe velocity of 1.0 mm/s. As shown, the frictional drag force dominates with the crack opening force being only 10-20 % of the drag force. We have a consistent value of total stalling force for all concentrations of agarose, $F_{Stall}$ $\sim$2.3nN (see Fig. 4-8(c)). This makes sense since the force generated by the acrosome should not depend on the concentration of agarose and thus the stall length becomes shorter when the opposing stresses become larger.

To be more rigorous, we must consider the shear stress dependence on the probe

geometry and the velocity. If agarose gel were an ideal homogeneous continuum, our shear stress measured at different conditions should yield the same stress values independently of the probe geometry and the measurement settings. However, agarose gel is a porous solid whose average pore sizes increase from 200nm to 500nm with decreasing concentration of agarose from 3 % to 1 %. Since the pore sizes are larger than the tip diameter, the interaction between the extending acrosome and the porous environment is much more complicated than what we measure with a macroscopic probe. Furthermore, even with the use of macroscopic probes which should not depend on the presence of the pores, we observe a weak trend that the shear stress increases with the decreasing diameter of the probe and increasing velocity of the probe (see Fig. 4-9(a) and (b)). These opposite effects make it more complicated to predict what the actual value would be for the acrosome of its diameter of 50-100nm in the limited case where velocity approaches zero. Unfortunately, we cannot use a smaller probe with the currently available load cell with the sensitivity of 1 mN. However, it is desired to perform more experiments using a smaller load cell with higher sensitivity.

### 4.3.2 Methylcellulose

As an independent check for the obtained force estimates with the agarose gel, we use MC solutions to mechanically slow down the reaction to get a lower bound estimate of the generated force. With increasing concentration of MC, we increase the drag on the extending acrosome and thus mechanically slow down the extension rate (see Fig. 4-10(a)). Unlike the case of agarose, the acrosomal bundle is able to extend to its full length with a finite final velocity (see Fig. 4-10(b)). For the acrosome to extend in a viscous medium at a finite velocity, the force generated by the acrosome must exceed the opposing viscous drag, and thus the maximum drag force exerted by the environment yields the lower bound of the acrosome force. From 5 % MC, we begin to notice that the extension rate toward the end becomes really small ($< 0.5$ $\mu$m/s) and a small fraction of cells stall before they reach their full length ($\sim$ 55-60 $\mu$m), implying that the drag force of the highly viscous environment is approaching

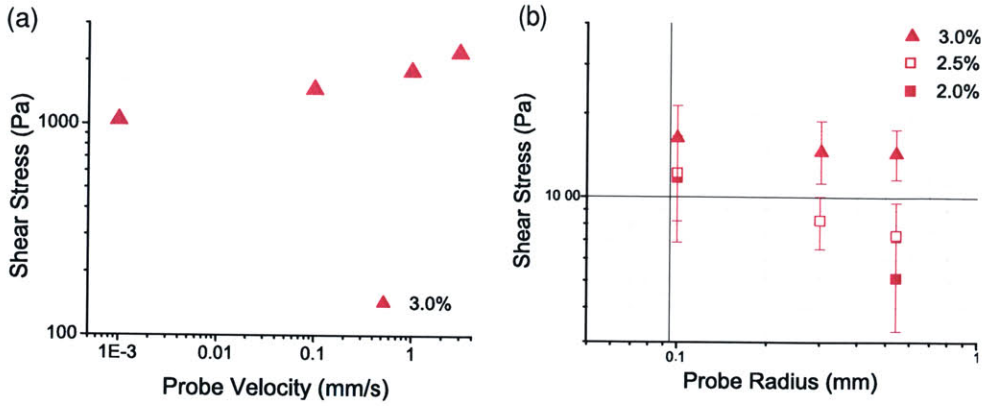


Figure 4-9: (a) The shear stress at various probe-velocity for the needle of $R_{Rod}$ =125mm shows a weak dependence. In actual experiments, the velocity of the acrosome bundle approaches zero right before it stalls and thus it is desired that we also perform the shear stress measurement at a very small velocity. With the change in probe velocity from 1mm/s to 1$\mu$m/s, the shear stress reduces only by a factor of 2. (b) The shear stress dependence on the probe radius is plotted for three different agarose concentrations. The stress increases with decreasing probe radius and the effect is more dramatic for a lower concentration of the agarose. At 3%, the shear stress is a very weak function of the probe radius. For our first approximation, we use the shear stress and crack stress values obtained for 3% agarose.

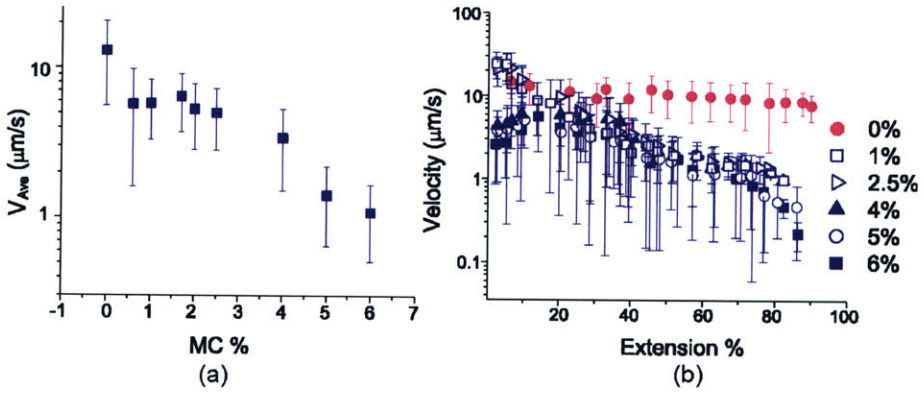


Figure 4-10: (a) With increasing concentrations of MC, the drag on the extending acrosome is increased, leading to a reduced extension rate. (b) Unlike the case of agarose, even at a very high concentration of agarose, the acrosomal bundle is able to extend to its full length with a finite final velocity. From 5 % MC, we begin to notice that the extension rate toward the end becomes very small ($<$ 0.5 $\mu$m/s).

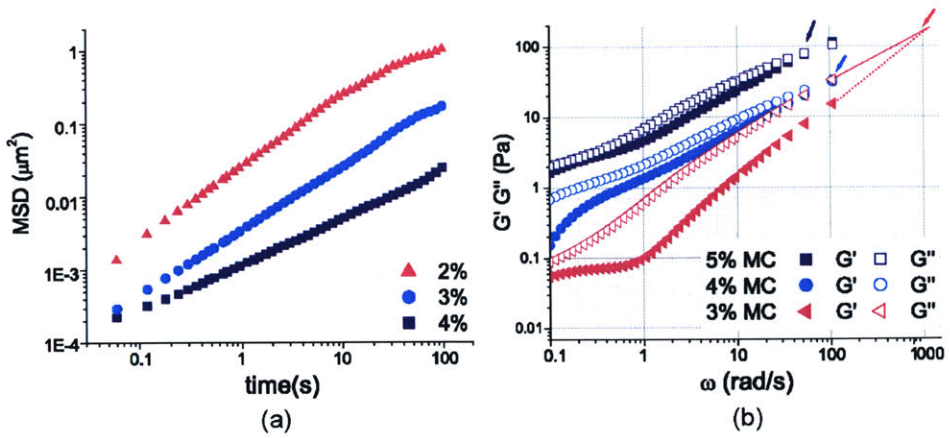


Figure 4-11: (a) MSD of 100nm particles in 2 %, 3 %, and 4 % MC solutions. A sub-diffusive material exhibits a ¡1 power law dependence. Purely viscous liquid exhibits a unit exponent (indicated with dotted magenta line). (b) MC solutions <6 % are predominantly liquid-like in the frequency range of 0.1-100 rad/s. The value of the crossover frequency at which the solution make a transition from a liquid-like state to a solid-like state becomes smaller with increasing concentrations of MC.

the acrosome force. Unfortunately, we are unable to make a MC solution beyond 6 % because the solutions become cloudy with tiny bubbles and particles that are impossible to remove. Therefore, we may obtain the maximum of the lower bound force from the data obtained with the highest concentration MC.

Since the tip diameter of the acrosomal bundle is only of the order of 50nm, we use micro-rheology to characterize the mechanical properties of the local environment. From the thermal motions of embedded particles of 100nm diameter, we obtain the MSD as a function of time (see Fig. 4-11(a)) and the elastic, $G'$, and loss, $G''$, moduli are determined from the complex shear modulus $\tilde{G}(s)$.

As shown in Fig. 4-11(b), the MC solutions at their concentrations lower than 5 % is predominantly "liquid-like" with G″ > G′ for the frequency range of 0.1-100 rad/s and thus we are interested in the viscosity of the medium as a characteristic property that is responsible for slowing down the extension. For many polymer solutions, the shear viscosity as a function of shear rate, $\eta(\dot{\gamma})$, measured from steady flow measurement is almost identical to complex viscosity as a function of angular frequency, $\eta^*(\omega)$, obtained from the linear oscillatory measurements, such that $\eta(\dot{\gamma}) = \eta^*(\omega)$.

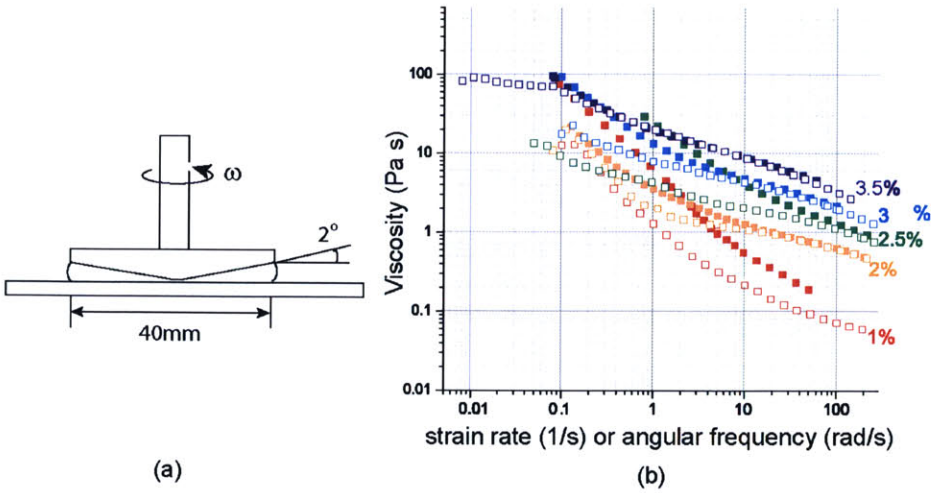


Figure 4-12: (a) A cone-plate geometry rheometer used for macro-rheology. (b) To test the applicability of the Cox-Merz rule in MC solutions, the shear viscosity as a function of shear rate, $\eta(\dot{\gamma})$, measured from macroscopic steady flow measurement (open symbols) is compared with the complex viscosity as a function of angular frequency, $\eta^*(\omega)$, obtained from the macroscopic linear oscillatory measurements (solid symbols). We find that only at high concentrations of MC (>2 % w/v) does the Cox-Merz rule hold and the relationship holds better at high shear rates and is valid in the shear rate regime of our interests, typically $\dot{\gamma} \sim 10$ - 200 $s^{-1}$.

This empirical finding is known as the Cox-Merz rule.

To test the applicability of the Cox-Merz rule for the MC solutions, we measure both dynamic and shear viscosities macroscopically using the cone-plate rheometer and discover that only at high concentrations of MC (>2 % w/v) does the Cox-Merz rule hold (see Fig. 4-12). Also, the relationship holds better at high shear rates and is valid in the shear rate regime of our interests, typically $\dot{\gamma} \sim$ 10-200 $s^{-1}$.

Provided that the Cox-Merz rule applies for the MC solutions at >2 % (w/v), we characterize the local viscosity of the MC solutions by calculating complex viscosity $\eta^*(\omega)$ determined from micro-rheology as $\eta^*(\omega) = G^*(\omega)/\omega = (G'^2 + G''^2)^{1/2}$ (see Fig. 4-13(a)). As shown in Fig. 4-13(b) for the case of 4 % MC, the dynamic viscosity measured from micro-rheology is always about 10-20 folds smaller than macroscopically obtained value.

Another issue to consider is whether the Stokes formalism is appropriate to use to

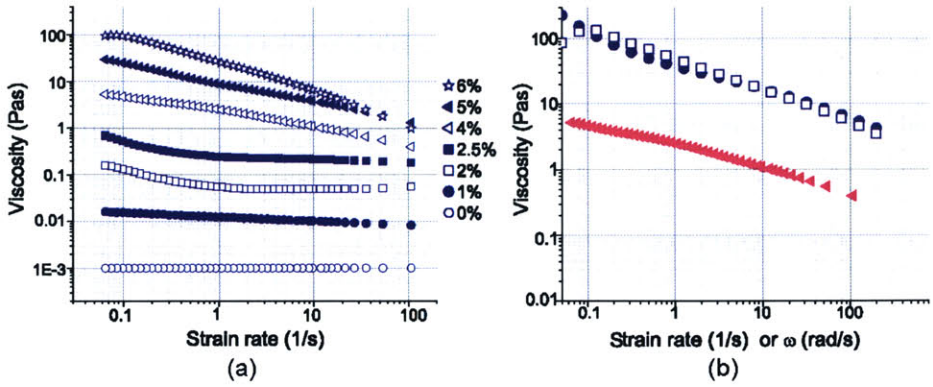


Figure 4-13: (a) The complex viscosity as a function of angular frequency, $\eta^*(\omega)$, obtained using the MPT technique with 100nm particles. The viscosities of the 1-4 % MC solutions are a very weak function of strain rate in the strain rate (or angular frequency) range of 1-200 $s^{-1}$. (b) The complex viscosity measured from micro-rheology (solid triangles) is about 10-20 folds smaller than macroscopically obtained values (open square: steady flow measurements, solid circle: linear oscillatory measurements) in all concentrations of MC (shown for the case of 4 % MC).

obtain the drag force against the extending acrosome. For a viscoelastic fluid, the drag force can be estimated using the Stokes equation, $F_V \sim 2\pi\mu_m x\upsilon/(ln(x/2R_d(x))-0.2)$, only in the limited case of viscous regime with Deborah number (De)$\ll$1. Deborah number, defined as $De \equiv \tau\omega$, characterizes how "liquid-like" the material is, where $\tau$ is the characteristic relaxation time, the longest time required for the elastic structure in the fluid to relax, defined as $\tau \sim 1/\omega_c$. From the experimental data, the crossover frequency $\omega_c$ is the frequency at which $G'$ and $G''$ crossover, separating elastic vs. viscous behavior of the material. As shown in Fig. 4-10(b), for 2.5 %, the crossover occurs at frequency $\omega_c$>200 rad/s and for 4 %, 5 %, and 6 %, $\omega_c$ 170 rad/s, 80 rad/s, and 0.7-0.8 rad/s, respectively. The corresponding relaxation time for 2.5 %, 4 %, 5 %, and 6 % are $\sim$ 0.005s, 0.006s, 0.013s, and 1.25s. To find the frequency range $\omega$ to calculate De, we first find what range of the strain rate $\dot{\gamma}$ is relevant in our experiments. We define the appropriate strain rate for the extending acrosome to be $\dot{\gamma} = \upsilon(x)/R_a(x)$ where $\upsilon(x)$ is the velocity of the acrosome which decreases as the length $x$ becomes longer, and $R_a(x)$ the average radius of the acrosome that thickens with an increasing length.

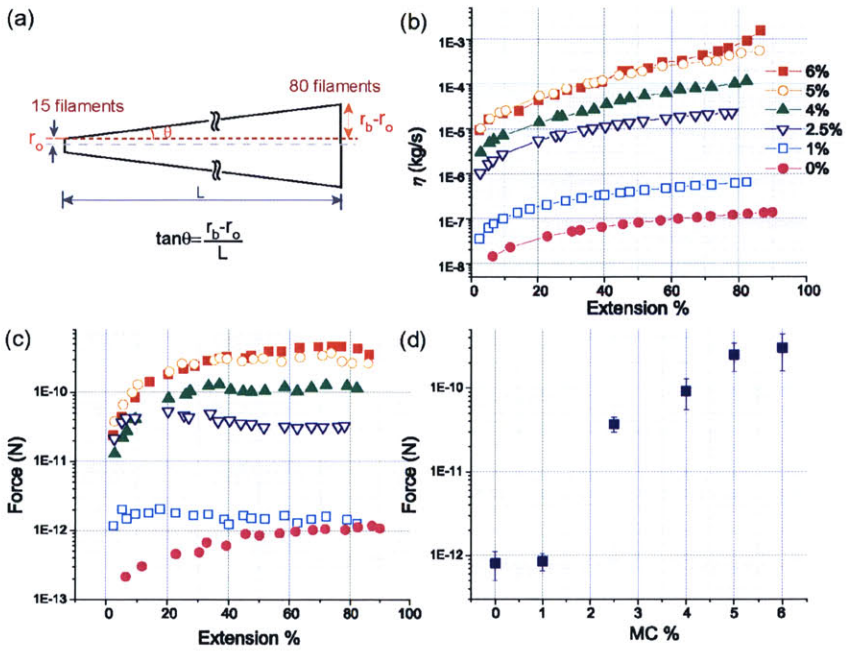


Figure 4-14: (a) The acrosomal bundle tapers from 80 filaments at the base to 15 filaments at the tip. (b) Drag coefficient $\eta = 2\pi\mu x/(\ln(x/2R_B(x)) - 0.2)$ during the extension for various concentrations of MC. (c) Drag force calculated based on Stokes equation shows that force the acrosome is pushing against is constant over the most of its length after a short transient period and the plateau values of the force increase with increasing concentrations of the MC solutions. (d) The average force increases with increasing MC concentrations and the highest value of these forces yields the maximum of the lower bound force estimate.

From the $v(x)$ data presented in Fig. 4-10(a) and $R_a(x) = 0.00073x + 24\times10^{-9}$ (see Fig. 4-14(a)), we obtain experimentally relevant ranges of angular frequencies (as $\omega = \dot{\gamma}$ in applying the Cox-Merz rule) for 2.5 %, 4 %, 5 %, and 6 % to be 20-830 $s^{-1}$, 15-170 $s^{-1}$, 10-150 $s^{-1}$, and 5-100 $s^{-1}$, respectively. The corresponding Deborah number ranges are then 0.12-4, 0.09-1, 0.09-1.8, and 4.5-130 for 2.5 %, 4 %, 5 %, and 6 %. Therefore, 6 % MC solution behaves more like the elastic solid and thus the Stokes formalism to characterize the drag force is not appropriate. The rest of the solutions >2 % (w/v) lie mostly in the viscous "liquid-like" regime and thus the Stokes equation can be used to obtain the drag force that resist the motion of the extending acrosome.

In calculating the drag coefficient, $\eta = 2\pi\mu x/(\ln(x/2R_B(x)) - 0.2)$, we take the

following into consideration: 1) the acrosomal bundle tapers, 2) viscosity $\mu$ is shear rate dependent, and 3) the shear rate $\dot{\gamma}$ changes during the extension because both the velocity and the radius are changing. We first calculate appropriate shear rate for $x$=0:60 $\mu$m. From Fig. 4-13(a), we then calculate a functional fit that represents the viscosity curve as a function of shear rate in the region of interest for each concentration of MC. Using the functional fit, we obtain corresponding $\mu$for every varying strain rate during the extension. Fig. 4-14 (b) shows the calculated drag coefficient as a function of extension %, where extension % is the extension length divided by the average total length 60 $\mu$m.

Interestingly, the force vs. extension % plot in Fig. 4-14(c) shows that the force the acrosome is pushing against is constant over the most of its length after a short transient period ($\sim$ 20-25 % of extension) and the plateau values of the force increase with increasing concentrations of the MC solutions. Fig. 4-14(d) shows the average force values at various concentrations of MC and 5 % MC yields the maximum of the lower bound estimate for the acrosomal force, $F_{Low} \sim$ 380 pN. This is about 17 % of the upper bound force obtained from stalling experiments and supports that our estimates are in a reasonable range.

Then, why should *Limulus* sperm produce this much force during the acrosomal reaction? The ultimate goal of the acrosomal reaction is to make a bridge between the egg and the sperm nucleus for successful fertilization. As illustrated in Fig. 4-15(a), *Limulus* egg features a very tough outer layer followed by a soft jelly-like material. The outer tough layer of $\sim$ 2 $\mu$m thickness is called basement lamina and beneath that is the 40 $\mu$m thick soft layer called the vitelline envelope (terminology after Dumont and Anderson, 1967). Therefore, the acrosomal reaction must produce sufficient pressure to penetrate through the protective layers during fertilization.

We perform a penetration test using the Zwick instrument with 100nm radius platinum wire. Our independent study on an agarose gel with different diameter probes shows that the initial puncturing pressure is conserved regardless of the probe size, validating the egg puncture test with the probe of a thicker diameter than the acrosome. As shown in Fig. 4-15(b), the probe deforms the egg surface before it

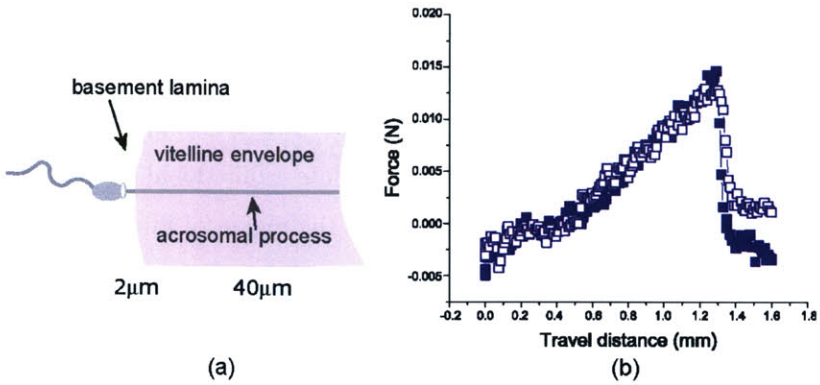


Figure 4-15: (a) When a sperm cell fuses its apical cap (acrosomal vesicle) on the surface of an egg, it must travel through two layers, basement lamina and vitelline envelope. (b) Force vs. displacement from the puncture test on *Limulus* eggs using 100nm radius platinum wire.

punctures at a consistent force for repeated measurements on 8 different eggs. From the initial slope prior to the puncturing, we approximate the elastic modulus of the egg to be $\sim$ 0.1Mpa by $E/R_{Rod}u$ where $u$ is the deformation. The puncturing pressure is calculated by $P_p = F_{Max}/\pi {R_{Rod}}^2$ and the average value from 8 different eggs is 0.45$\pm$ 0.06 MPa. Based on the force estimate from the stalling experiment, $F \sim$ 2.3nN, the imposed pressure on the egg by the tip of the acrosome is $\sim$ 1.3MPa, which is larger than what takes to puncture the egg. Interestingly, studies by Shoger et al. [50] have shown that the basement lamina features regularly spaced thru canales (2 $\mu$m apart) and the sperm cells sit right on the pores in an evenly distributed manner by means of their ruptured apical cap (see Fig. 4-15(b)) such that the acrosomal bundle travels through the canal without having to physically penetrate the tough layer. If this were the case, it will take even less pressure to penetrate into the egg than what we estimate from the puncture test.

# Chapter 5

# Relating $\mu$-structure to rheology of a bundled and cross-linked F-actin network *in vitro*

## 5.1 Introduction

F-actin is one of the most important participants in maintaining the mechanical integrity of eukaryotic cells. In vivo, actin filaments rarely exist as isolated single filaments but instead associate into bundles or networks, in concert with more than 60 different actin binding proteins (ABPs), to influence cell shape, division, adhesion, and motility [27, 3, 62, 7]. The elastic modulus of cytoplasmic actin gels is estimated to be of order 100 - 1000 Pa [16] and the gel must be able to sustain shear stresses of up to 1000 Pa for proper cell functions [4]. This large elasticity cannot result exclusively from a network of actin alone; in vitro, solutions of entangled actin filaments are weak elastic solids. For example, a solution of actin filaments at a concentration of 24 $\mu$M has an elastic modulus of only 0.1 Pa and breaks under a shear stress of less than 0.1 Pa [18, 20]. Therefore, the properties of the actin cytoskeleton must be regulated predominantly by ABPs. Modest changes in the concentration of ABPs can significantly modify the structure of the network as they can both bundle and cross-link the actin filaments. These structural changes can lead to concomitant change in the mechanical properties, dramatically enhancing the mechanical rigidity [24, 40, 63, 52, 68]. The changes in structure occur over a large range of length scales, ranging from a few nano-meters, the size of an ABP, to several microns, the length

of an individual actin filament. The dearth of techniques that probe the structure and properties over this range of length scales has limited our ability to determine the modifications due to the ABPs and to identify their critical contributions. As a result, a quantitative understanding of how the changes in mechanical stiffness are correlated with structure remains elusive.

In this paper, we probe the changes in structure and mechanical properties of a F-actin network as a function of ABP concentration. We use electron microscopy (EM) to measure structural changes on the nano-meter scale and confocal microscopy to measure structural changes on the micro-meter scale. We exploit the technique of multi-particle tracking (MPT), using small non-binding particles, to directly probe the variations in mesh size with changing ABP concentration, and compare the results with the analysis of images obtained with confocal microscopy. Moreover, we employ MPT to probe the local mechanical response by using particles which bind to the network, and we correlate this with measurements of the bulk rheological properties. We thereby demonstrate the versatility of the MPT technique in providing the local structural and mechanical information, provided the data is interpreted with care, and we use the MPT results to probe the properties of cross-linked actin networks. By comparing our data to predictions of a theoretical model, we show that the linear elasticity of the composite network directly reflects the properties of individual actin filaments or bundles.

We use the ABP, scruin, which simultaneously bundles and cross-links the actin filaments. *In vivo*, scruin locks over 80 actin filaments to form an ordered crystalline bundle that functions as a mechanical spring in the acrosomal process in the sperm of *Limulus polyphemus* (horseshoe crab) [42, 49]. EM-derived structure shows that this acrosome bundle is an extensively cross-linked composite of actin filaments where scruin-CaM (calmodulin) heterodimers are bound to every actin subunit with its stoichiometric ratio of 1:1 (scruin: actin) [43, 47]. Scruin binds pairs of adjacent actin subunits in the same filament [43]; scruin makes a variety of contacts with neighbouring scruin molecules on different filaments to form a tight crystalline bundle. The Young's modulus, $E$, of a scruin mediated actin bundle in vivo is similar to that

of single actin filament, implying that scruin bonding is stiffer than actin [48].

In contrast, actin filaments polymerized in the presence of scruin *in vitro* form an isotropic, disordered three-dimensional network of rigidly bundled and cross-linked F-actin. The scruin cross-links are both rigid and irreversible; as a result, the compliance of the network is completely determined by that of the actin filaments, unlike other cross-linking proteins such as filamin or $\alpha$-actinin [63]. Thus, the actin-scruin composite network is an excellent model system with which to study the complex relationship between the microstructure and the macroscopic mechanical properties, and the physics of cross-linked semi-flexible polymer networks.

## 5.2 Materials and methods

### 5.2.1 Protein preparation

#### Actin

G-actin solutions are prepared by dissolving lyophilized G-actin in de-ionized water and dialyzing against fresh G-buffer (2 mM Tris HCl, 0.2 mM ATP, 0.2 mM $CaCl_2$, 0.2 mM DTT, 0.005 % $NaN_3$, pH 8.0) at 4°C for 24 hrs; the buffer is replaced with fresh G-buffer every eight hrs. Solutions of G-actin are kept at 4°C and used within seven days of preparation. Actin polymerization is initiated by adding F-buffer (2mM Tris HCl, 2mM $MgCl_2$, 100mM KCl, 0.2mM DTT, 0.2mM $CaCl_2$, 0.5mM ATP, pH 7.5) and mixing gently.

#### Scruin

Scruin is purified from the acrosomal process of *Limulus* sperm following the protocol by Sun et al. [51]. In the presence of high calcium, a bundle of actin filaments cross-linked by scruin:CaM heterodimers (Hereon, we use the term "scruin" to represent scruin:CaM heterodimer) extends from the head of the sperm to form a 60 $\mu$m-long finger of membrane, called the acrosomal process. The extended acrosome bundles are sheared from the cell body and then separated from the nuclei and flagella by centrifugation. The membrane surrounding the acrosome is removed with a mild detergent, HECAMEG (38mM Methyl-6-O- (N-heptylcarbamoyl)-$\beta$-D-glucopyranoside). Scruin

is solubilzed from the bundle by addition of 1M $CaCl_2$ and purified further by filtrations through a series of size exclusion column (AcA4), ion exchange column (MonoQ), and another size exclusion column (Superose 12). Fractions containing scruin are run on a SDS-PAGE (with a 3 % stacking gel and a 12 % resolving gel) to select the fraction of the best quality. The purified samples are stable at 4°C for about two weeks. Prior to experiments, scruin is clarified by spinning at 90,000 g for 20 min, and its integrity is checked with SDS-PAGE. Protein concentrations are determined either by the Bradford assay (using BSA as a standard) or by absorbance at 280 nm using an extinction coefficient of $1.68 \times 10^5$ $M^{-1}cm^{-1}$.

### 5.2.2 Multiple-particle tracking

Micron-sized tracer particles are added to the solution of G-buffer, F-buffer, and scruin. Immediately after addition of G-actin, the solution is gently mixed and transferred into a 5mm×10mm×1mm glass chamber. The chamber is sealed with high-vacuum grease to prevent evaporation and the sample is equilibrated for 1 hr at 25°C. We image approximately one hundred spheres per field of view with the bright field optics on an inverted microscope, and record their dynamics at 30 frames per second using a CCD camera with a shutter speed of 0.5 ms [8, 25]. Particle centers are detected in each frame to a resolution of ~20 nm and the time evolution of each particle position is determined [9]. To avoid wall effects, we image 100 $\mu$m into the sample. The particles remain in the field of view for at least 90s and we calculate the mean-squared displacement $\langle \Delta x^2(\tau) \rangle$(MSD) [60] of the individual particles undergoing thermal motions. Several thousand frames are captured, ensuring good statistical accuracy for time scales up to one hundred times the frame rate.

Thermally driven dynamics of the embedded particles depends sensitively both on the microstructure and the nature of the coupling between the particles and the network. When the particle radius, $a$, is significantly larger than the average mesh size of the network,$\xi$, or when the particles are chemically bound to the network, the particle motion probes the local mechanical response [10]. In this case, MSD of individual particles in the field can be related to the frequency-dependent linear

moduli using a generalized Stokes-Einstein relation to extract frequency dependent elastic and loss moduli; this technique is known as one-particle (1-P) microrheology [44, 33]. In cases where the particle size is much larger than all structural length scales, 1-P microrheology correctly captures bulk mechanical response. However, in materials with structural length scales similar to that of the particle size, the response probed by individual particles may not correspond to the bulk mechanical properties [66]. To circumvent this problem, we examine the correlated motions of pairs of particles to examine only the stress fluctuations that propagate at large length scales; this technique is known as two-particle (2-P) microrheology [8], and correctly probes bulk mechanical properties.

As the embedded particle radius approaches the typical mesh size of the material, $\xi \sim a$, the thermal motion of the particles can be used to probe the local microstructure, assuming that the particles are not chemically bound to the network [60, 66, 61, 35]. The particles explore the local structure diffusively at short time scales while the steric and elastic constraints imposed by the network affect the dynamics of the network at longer time; thus, a plateau in the MSD of individual particles should reveal the local pore size, $\xi = \sqrt{\langle \Delta x^2(\tau) \rangle} + a$ for large $\tau$[60].

In this study, we use 1 $\mu$m-diameter particles coated with either poly-ethylene glycol (PEG) or bovine serum albumin (BSA) to elucidate both the network microstructure and the local elasticity using MPT. The PEG coating prevent scruin adsorption on the particles, enabling them to probe the changes in network microstructure [61]. Although the BSA-coating is generally known to reduce the adsorption of some proteins to colloidal surfaces, scruin has been shown to readily bind to the BSA-coated particles [61], making the particles adhere to the bundles. The bound particles are sensitive to the changes in local rigidity and thus can be used as a probe to measure the elasticity of the bundled network. Thus we use the PEG-coated particles to probe the microstructure of the network and the BSA-coated particles to probe the mechanical response, using both 1-P and 2-P microrheology.

### 5.2.3 Bulk rheology

The bulk mechanical response of the networks is measured with a stress-controlled rheometer (CVOR, Bohlin Instruments) with a 40 mm parallel plate geometry and gap of 140 $\mu$m. The maximum applied strain, $\gamma$, is maintained at sufficiently low values, typically <0.02 to ensure that the measurements are in the linear elastic regime. We measure the frequency dependent elastic modulus, $G'(\omega)$, and loss modulus, $G''(\omega)$ in the frequency range of 0.06 - 30 rad/s. Within this range, the mechanical response of all networks is dominated by a frequency independent elastic modulus, $G'(\omega)=G_0$. Additionally, we probe the elastic response as a function of strain, $\gamma$ at a fixed frequency =1 rad/s, to determine the range of the linear response by determining $\gamma_{crit}$, the strain at which the mechanical response becomes nonlinear.

### 5.2.4 Confocal fluorescence microscopy

Confocal fluorescence microscopy is used to visualize the structure of the bundled and cross-linked F-actin network and to obtain independently of the MPT method. We deposit a 3 $\mu$l drop of 6.6 $\mu$M Texas-Red phalloidin (T7471, Molecular Probes, Eugene, OR) in methanol on a glass (No. 1.5) bottomed chamber ( P35G-1.5-14-C, MatTek Corporation, Ashland, MA), and allow it to dry at least for 1 hr. The actin-scruin mixture is prepared by adding F-buffer at various concentrations of scruin, and the samples are immediately loaded on top of the dried Texas Red dye such that the final ratio of the dye to the sample is 1:200 (v/v). The sample is then enclosed by placing a coverslip over a spacer, a thick layer of vacuum grease laid around the sample. The actin-scruin mixture is allowed to polymerize for 1 hr at room temperature (~25°C) and examined using a Zeiss LSM 510-Meta confocal microscope. Laser excitation at $\lambda$=543nm is used with LP 560 filter and HFT 488/543 beam splitters. For 3D imaging, a stack of 20-100 frames is collected with an interval of 100nm between adjacent slices. Fluorescent images are deconvolved using Huygens2 software (Scientific Volume Imaging B.V., Netherlands) and the images are assembled to obtain a 3D projection using Imaris3 software (Bitplane, Switzerland). The mesh size is determined by measuring the peak-to-peak distance in the intensity profile

obtained across fluorescent images.

### 5.2.5 Electron microscopy

A 10 $\mu$l mixture of actin-scruin, polymerized at room temperature for 1 hr, is transferred to 400-mesh carbon coated nickel grids (Electron Microscopy Sciences, Fort Washington, Pa). After waiting for 30s, the samples are negatively-stained with 1 % uranyl acetate (UA) by passing drops of freshly prepared UA solution across the grid. The stained grids are air-dried and examined using a Philips EM410 transmission electron microscope. The negatives are scanned to digital images in Tiff format and the thicknesses of the bundles are measured using Openlab software (Improvision, Lexington, MA).

### 5.2.6 Co-sedimentation assays

#### Binding and polymerization assay

Co-sedimentation assays are performed at high speed to check the degree of F-actin polymerization and scruin binding. Mixtures of actin and scruin at various concentrations are incubated for 1 hr at 25°C and then centrifuged at 200,000 g for 30 min at 4°C in a TLA100 rotor (Beckman, Palo Alto, CA). A sample of 11.9 $\mu$M actin is also polymerized and ultra- centrifuged as a control. The pellets are resuspended in 1×F-buffer. Both supernatants and pellets are run on a SDS-polyacrylamide gel (3 % stacking and 12 % resolving) and the gel is stained with 0.2 % Coomassie Brilliant Blue R-250 to visualize the protein bands in the gel.

#### Bundling assay

The assay for bundling is virtually identical to the binding assay except that low speed sedimentation is used. Typically, bundles sediment at 10,000 g in 15 min but almost no F-actin sediment at this speed. It is important to include a control sample of F-actin only. After incubating for 1 hr at room temperature, 50 $\mu$l of actin-scruin mixture is spun at 12,000 g for 15 min using a table top centrifuge (3200, Eppendorf, Westbury, NY). The supernatant is carefully pipetted out of the

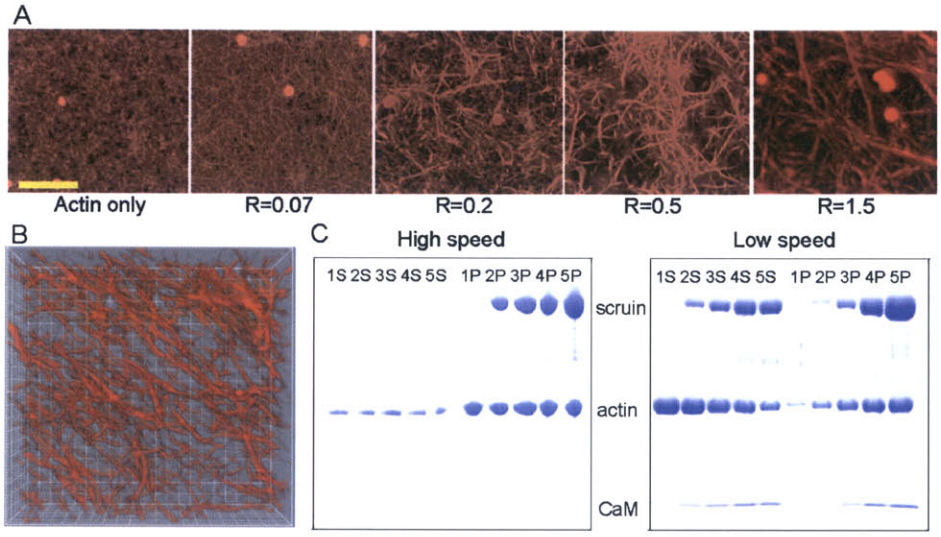


Figure 5-1: Changes in the degree of bundling at varying $R$. (A) Confocal images of an F-actin:scruin network at various $R$. The right most image is an assembled 3D projection of 50 images with 100nm intervals. Scale bar measures 10 $\mu$m (B) 3D deconvolved image of a 1:2 (S:A) network. Each grid measures 1m (C) Scanned image of a SDS-polyacrylamide gel. The sample numbers, 1, 2, 3, 4, and 5, correspond to $R$=0, 0.07, 0.2, 0.5, and 1, respectively, at a fixed $c_A$=11.9 $\mu$M, and (S) and (P) represent supernatants and pellets, respectively, after centrifugation. High speed co-sedimentation assay indicates that the F-actin density is unaffected by the presence of scruin and all of scruin binds to F-actin. Low speed assay shows the degree of bundling; although all scruin binds to F-actin, not all of the scruin-decorated F-actins assemble into thick bundles.

tube and any remaining supernatant is removed by inverting the tube and letting the liquid drain. The pellet is the re-suspended in F-buffer. Both supernatants and re-suspended pellets are analyzed by SDS-PAGE.

## 5.3 Results

In the current study, we make direct measurements of the network microstructure with confocal microscopy, EM and MPT. To characterize the structure, we determine the distribution of pore sizes and bundle thicknesses as the ratio of scruin to actin concentration, $R = c_S/c_A$, is varied. Co-sedimentation assays at both high and low speed are performed to confirm that the addition of scruin has no effect on the actin filament density but only enhances the bundling of filaments. We measure the network elasticity with MPT and bulk rheology. We compare our results to the predictions of a model of entropic elasticity for semi-flexible polymer networks, and we show that the bulk properties of the network are directly related to the properties of individual bundles and filaments at the length of the mesh size.

### 5.3.1 Evolution of pore structure

Confocal fluorescence microscopy with the labelled actin indicates that when scruin is added, actin filaments form bundles whose thickness increases with increasing concentration of scruin as shown in Fig. 5-1(A); simultaneously the pore size of the network becomes larger. The high speed co-sedimentation assay confirms that the majority of actin is polymerized and that the degree of actin polymerization is independent of the presence of scruin, and the actin filament density in the network remains constant regardless of the amount of scruin in the sample (see Fig. 5-1(C)). This observation is in contrast with other ABPs such as profilin, which control actin assembly by altering the concentration of G-actin at which polymerization to F-actin is initiated [45, 65]. Moreover, all the scruin co-sediments with F-actin, suggesting that scruin has a high affinity for filamentous actin. The low-speed co-sedimentation assay characterizes the amount of scruin in the pelleted bundle and indicates that more filaments form bundles as the concentration of scruin is increased (see Fig. 5-1(C)). However, this

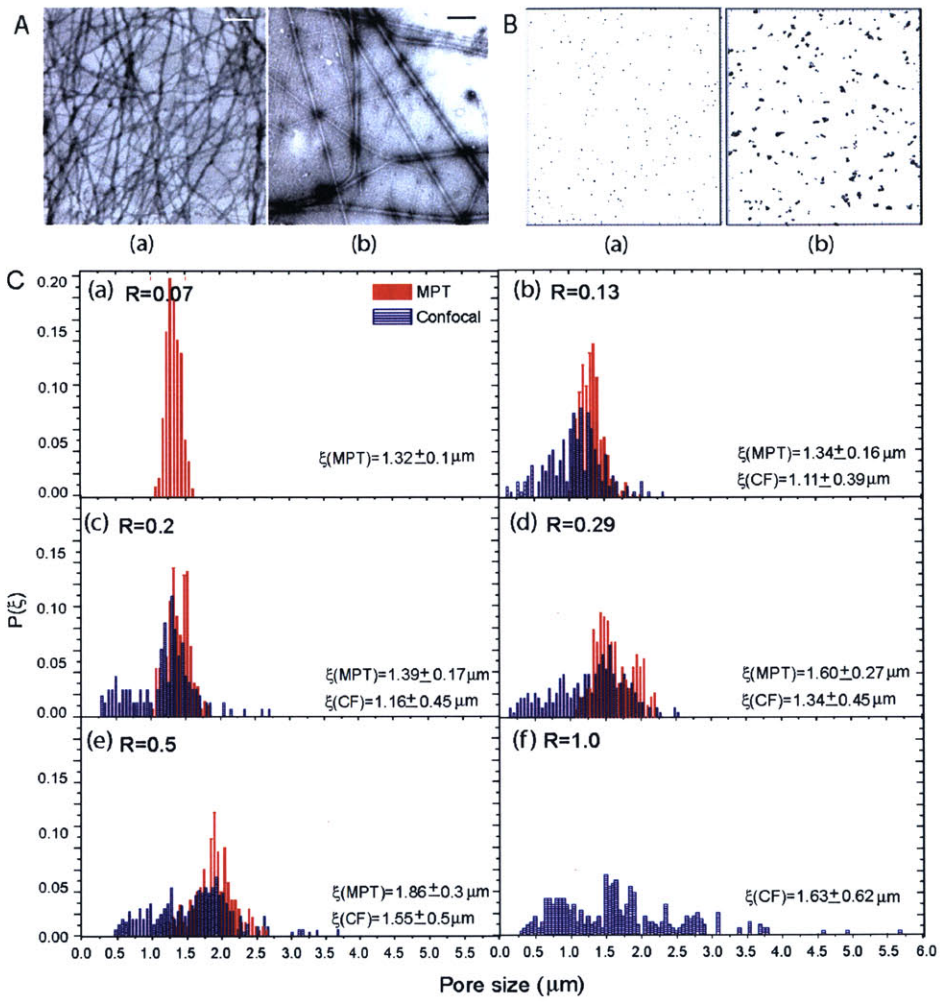


Figure 5-2: Characterization of the bundle thickness, $D_B$, and pore size,$\xi$, distribution at various $R$. (A) EM images of the (a) actin only and (b) $R$=1 sample. Scale bar measures 200nm. (B) 2D map of the particle trajectories to demonstrate $\xi$ and the degree of heterogeneity at (a) $R$=0.03 (b) $R$=1. Scale bar measures 1 $\mu$m. (C) The distribution of pore sizes at various $R$ for $c_A$=11.9 $\mu$M measured with MPT (solid red) and confocal microscopy (striated blue). We observe both and its standard deviation ($\sigma$) increasing as $R$ increases (a-f).

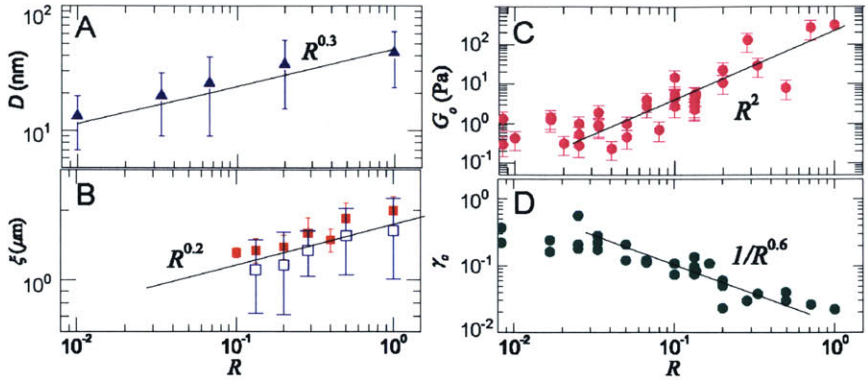


Figure 5-3: The bundle thickness (A), mesh size (B), elastic modulus (C) and critical strain (D) as a function of $R$ at $c_A$=11.9 $\mu$M. (A) The average $D_B$ at various $R$ is measured from the digitized EM images and shows $D_B \sim R^{0.3}$. A single actin filament is ~7nm in diameter and $D_B$ becomes as large as 65nm at $R$=1. (B) $\xi$ is measured using both MPT (solid squares) and confocal imaging (open squares). Results show that $\xi$ at $R$=0.1 is two times larger than that predicted for an entangled actin network and follows the scaling of $\xi \sim R^{0.2}$. (C) $G_0$ is measured using bulk rheology and the best fit for the data follows $G_0 \sim R^2$ (solid line). (D) The strain at which we observe the onset of non-linearity, $\gamma_{crit}$, of the actin:scruin composite networks at various $R$, showing a scaling of $\gamma_{crit} \sim R^{-0.6}$

assay is not able to differentiate between the effects of bundle thickening and the increase in number of bundles. Instead, we use confocal imaging to show that the number of single filaments decreases while the bundles thicken with increasing scruin concentration. At a low concentration of scruin (low $R$), it is more probable to form random crossover points between two filaments, leading to small loose bundles with irregularity in their structure as evidenced in EM images. As $R$ is increased, more tightly bound individual bundles become visible in an otherwise largely homogeneous network of actin filaments; beyond a critical $R$, the bundles themselves become cross-linked by means a variety of scruin-scruin interactions. The bundle thickness, DB, at various R is visualized by transmission electron microscopy (TEM) of negatively stained bundles of actin (see Fig. 5-2(A)), and we find $D_B/D_0 \sim R_x$ where $x$=0.3 (see Fig. 5-3(A)).

We quantify the pore size distribution using both MPT and confocal microscopy. MPT is conventionally used to quantify the local elasticity, viscosity, and diffusivity of soft materials such as gels and entangled solutions [44]. This technique also offers a

new method to characterize the organization of polymers in solution. The distribution of particle MSD is mapped onto a 2D plane to study the degree of heterogeneity, and the magnitudes of the MSDs are used to determine the pore size distribution (see Fig. 5-2(B)). We find that the average pore size, $\xi$ increases from 1.3 to 1.9 $\mu$m as $R$ varies between 0.1 and 0.5; furthermore, the degree of heterogeneity in the distribution also increases with increasing $R$ as indicated by the increased width of the distributions (see Fig. 5-2(C)). The distributions of pore sizes determined by analyzing confocal images, shown by the blue columns in Fig. 5-2(C), show a similar trend to those determined with MPT; however the average values obtained from the confocal images are consistently $\sim$16 % lower than those obtained from MPT. The difference arises because randomly cut cross-sections of a three-dimensional object will always be smaller than the maximum diameter of the pore. In addition, while the MPT method cannot measure pores smaller than the particle size (1 $\mu$m), the confocal imaging method is limited by the resolution of the optics and thus expands the distribution curve to smaller sizes. Therefore, the MPT measurements overestimate $\xi$ while the confocal imaging underestimates it. In the absence of any quantitative characterization of this difference, we use the average of these two independent measurements to determine $\xi$. Our experiments show that at $R$=0.1, $\xi$ has increased by a factor of two over that predicted for a purely entangled actin solution; moreover we find that the mesh size continues to increase as $R$ increases, $\xi \sim R_x$, where now $x$=0.2 (see Fig. 5-3(B)).

### 5.3.2 Mechanical Response

We measure the mechanical response of the composite network using both microrheology and bulk rheology techniques. The elastic moduli obtained from both the 1-P and 2-P microrheology with BSA coated particles are in good agreement with the modulus obtained with bulk rheology. Nevertheless, the results suggest that the 2-P microrheology is a better measure of the bulk property of the network (see Fig. 5-4). Two-particle microrheology probes the behavior over a larger length scale; it also eliminates variations in local mechanical response caused by differences in the coupling between the embedded particles and the network.

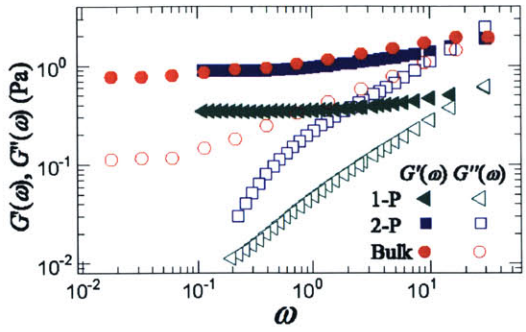


Figure 5-4: G′(ω) (solid symbols) and G″(ω) (open symbols) at $c_A$=11.9 $\mu$M and $R$=0.03 measured with 1) one-particle, 2) two-particle microrheology, and 3) bulk rheology. While the elastic moduli, $G_0$, measured with both 1-P and 2-P microrheology with BSA-coated particles match well with the bulk measurement, 2-P microrheology shows an excellent agreement with the bulk rheology; 2-P microrheology is insensitive to local changes originating from the coupling between the network and the particles, allowing to measure the long wavelength rheology.

Composite actin-scruin networks are predominantly elastic gels where the elastic modulus, G′(ω), shows little frequency dependence in the range of =0.03-30 rad/s as shown in Fig. 5-4. Thus, we can characterize these networks with a single low frequency plateau elastic modulus, $G_0$, measured at $\omega$=0.6 rad/s. We determine changes in both $G_0$ and the strain at which the network response becomes nonlinear, $\gamma_{crit}$, as a function of filament cross-linking and bundling as we increase $R$ at fixed $c_A$. The effects on the mechanical properties are significant particularly for $R$ >0.03; at $c_A$=11.9 $\mu$M, $G_0$ changes by four orders of magnitude from 0.1 to 300 Pa when $R$ is varied from 0.01 to 1. We find $G_0 \sim R^2$ for fixed $c_A$ and for $R$ >0.03 as shown in Fig. 5-3(C). Associated with the increase of Go is a decrease in crit from 0.4 to 0.04 as R is varied from 0.04 to 1. We find $\gamma_{crit} \sim R^{-0.6}$. As the ratio of scruin to actin decreases, we observe a transition from a highly bundled and densely cross-linked composite network to a very weak network of actin filaments at $R$ ~0.03; the elastic modulus of this weak network is only slightly greater than that of a solution of entangled actin filaments at the same $c_A$. At concentrations of scruin below this bundling threshold, the gel retains its isotropic nature with a very slow change in its elastic modulus as the scruin concentration decreases [65].

## 5.4 Discussions

In this paper, we report the changes observed in mechanical response and in local microstructure upon formation of a bundled and cross-linked actin network with increasing concentration of scruin, a rigid ABP. The modification of the microstructure arises from the fact that scruin has two types of interactions, scruin-actin and scruin-scruin interactions; scruin decorates individual actin filaments, and simultaneously forms adhesive patches which can interact with one another either to form bundles of multiple filaments or to form cross-links between bundles of filaments, thereby forming a solid gel. To correlate the changes of the microstructures induced by the ABP to the mechanical properties of the network, we relate the elasticity of the cross-linked and bundled network to the properties of constituent individual bundles and filaments.

In the absence of any ABPs, the elasticity of single actin filaments, and their entangled solutions, is purely entropic [37]. In the presence of ABPs which lead to cross-linking, the elasticity of the resultant network of semi-flexible filaments can also be entropic in origin [18, 30]. We can theoretically relate the elasticity of the network to the elasticity of single entropic filaments. To accomplish this, the cross-linked network is modelled as a collection of thermally fluctuating semi-flexible polymers. For such a network, the elastic modulus is (see Fig. 5-5) [30]

$$G_0 \sim \kappa_0^2/(k_B T \xi^2 l_c^3) \tag{5.1}$$

where $\kappa_0$ is the bending rigidity of a single filament, $\xi$ the network pore size, and $l_c$ the distance between cross-links. Using the same model, we can also calculate the critical strain $\gamma_{crit}$ at which the mechanical response becomes non-linear, which is (see Fig. 5-5)

$$\gamma_{crit} \sim \frac{k_B T}{\kappa_0} l_c. \tag{5.2}$$

For our actin-scruin composite networks, bundling and cross-linking have a large effect on both the bending rigidity, $\kappa$ and $l_c$; this provides a means of exploring the

relationship between microscopic structure and mechanical response of the bundled and cross-linked network. To accomplish this, we investigate the changes in $G_0$ and $\gamma_{crit}$ as a function of $R$ at a fixed actin concentration of $c_A$=11.9 $\mu$M. Due to the compact nature and the large number of scruin-scruin interactions between adjacent filaments, scruin mediated actin bundles behave like homogeneous elastic rods with a Young's modulus, $E$, similar to that of a single actin filament (18). For a linear, elastic, and isotropic rod, $\kappa \sim D^4$ where $D$ is the diameter (35). Therefore, we infer that the bending rigidity of the composite bundle is $\kappa_B \sim \kappa_0(D_B/D_0)^4$ where $D_B$ is the bundle diameter, $D_0$ the diameter of a single actin filament, and $\kappa_0$ the filament bending rigidity. We must also account for the effect of bundling on the mesh size. From the co-sedimentation assay, we know that the total number of actin filaments remains constant, independent of $R$. Thus, as the bundles thicken, the average spacing between bundles must increase. Therefore, as $D_B$ increases, the effective $\xi$ of the network also increases, giving $\xi \sim D_B/\sqrt{c_A}$. From our EM measurements, we determine the increase in bundle thickness, $D_B \sim D_0 R^x$. This allows us to determine the variations in both and as a function of bundling. For the bending rigidity, we find $\kappa_B \sim \kappa_0 R^{4x}$ where $x$ is the bundling exponent. For the mesh size, we find $\xi \sim D_0 R^x/\sqrt{c_A}$. Furthermore, for a densely cross-linked network, $l_c$ is proportional to the entanglement length, $l_e$ [46], $l_c \approx n' l_e$; moreover, as the degree of cross-liking increases, we expect $n'$ to decrease, and thus we take $l_c \sim n l_e R^{-y} \sim n\xi^{4/5} l_p^{1/5} R^{-y}$ where $y$ is a cross-linking exponent. Using Eq. 5-1, we predict the elastic modulus of the bundled network as a function of $R$,

$$G_0 \sim \frac{\kappa_0^2}{\xi^2 l_c^3} \sim c_A^{11/5} R^{(6x+15y)/5}. \tag{5.3}$$

This scaling relation allows us to consider the competition between bundling and cross-linking in determining the effects of elastic properties in modifications of morphology of the networks. We can directly measure the bundling exponent, $x$, by imaging the actin-scruin networks. By direct measurements from the EM images, we determine the scaling of the bundle thickness, $D_B \sim D_0 R^x$, with $x$=0.3 (see Fig. 5-3(A)). This is in good accord with our determination of the bundling exponent

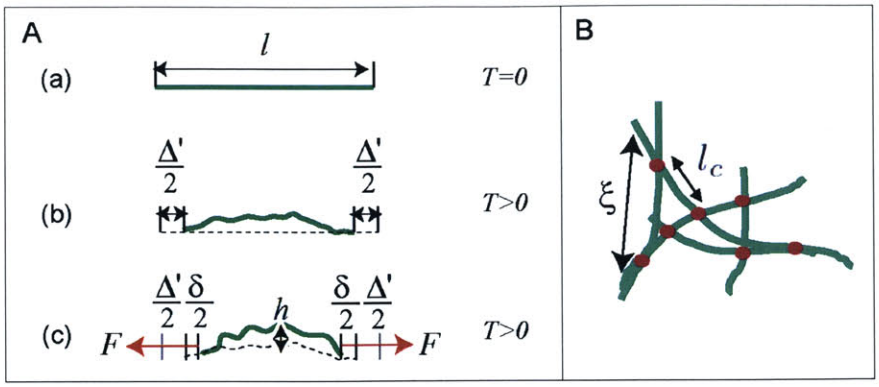


Figure 5-5: **Derivation of elasticity of a semi-flexible polymer** (A) A single inextensible semi-flexible filament with a contour length of $l_c$: (a) at absolute zero temperature (T=0) where thermal effects vanish, the end-to-end distance, $l$, of a semi-flexible polymer equals to $l_c$. (b) for T>0, the filament undergoes thermal fluctuation of a magnitude $h$, and $l$ contracts by $\Delta'$ due to the thermal bending such that $l = l_c - \Delta'$. The corresponding bending energy is $U_B \sim \kappa_0 l(h/l^2)^2$ where $\kappa_0$ is the filament bending rigidity. (c) In the presence of an applied extensional force, $F$, the contracted filament extends by $\delta$ with the stretching energy of $U_F \sim Fl\varepsilon \sim Fh^2/l$ where $\varepsilon$ is the net stain of the filament due to both the bending and stretching, $\varepsilon = (\Delta' - \delta)/l_c$. The elastic energy due to bending and stretching must balance the thermal energy by equipartition such that $U_B + U_F \sim (\kappa/l^2 + F)\varepsilon l \sim k_B T$. This can be re-written for $\varepsilon \sim (l^2/l_p - Fl^4/k_B T l_p^2)/l_c$ with the persistence length, $l_p = \kappa/k_B T$, yielding the lateral displacements $\Delta' \sim l^2/l_p$ and $\delta \sim Fl^4/k_B T l_p^2$; thus, the linear force-extension is $F \sim (\kappa^2/k_B T l^4)\delta$. (B) For a cross-linked network characterized by a pore size $\xi$, the stress $\sigma$ is defined by $\sigma \sim F/\xi^2$ and the imposed strain is $\gamma \sim \delta/l_c$ where $l_c$ is now the distance between cross-links. This leads to the network elastic modulus $G' \sim \sigma/\gamma \sim \kappa^2/(k_B T \xi^2 l_c^3)$.

from the measurements of the scaling of the mesh size using both confocal imaging and MPT, where we find $\xi \sim D_0 R^x$ with $x$=0.2 for $R > 0.03$ at a fixed $c_A$ (see Fig. 5-3(B)). Thus, we show our measurements at the nano-meter scale made with EM correlate well with our measurements at the micro-meter scale made with optical techniques.

We cannot independently determine the value of the cross-linking exponent, $y$. Instead, we use our measurements of the $R$ dependence of $G_0$ to determine a value for $y$ and compare this to the resultant $R$ dependence of $\gamma_{crit}$. We observe $G_0 \sim R^2$ in our bulk measurements, as shown in Fig. 5-3(C); thus, Eq. 5-3 yields the cross-linking exponent $y = 0.58$ using $x = 0.2$. The fact that $y > x$ may imply that the effects of cross-linking are stronger than those of bundle formation in our in vitro actin-scruin

composite networks. Using Eq. 5-2, we obtain

$$\gamma_{crit} \sim \frac{k_B T}{\kappa_0} l_c \sim c_A^{-2/5} R^{-(12x+5y)/5} \sim c_A^{-2/5} R^x. \tag{5.4}$$

Using the measured value of $x$ and the value predicted for $y$, we find $z \sim$ -1.1. By comparison, we measure $\gamma_{crit} \sim R^{-0.6}$ as shown in Fig. 5-3(D). Given the inherent uncertainties and the large exponents, this agreement is quite reasonable. Thus, our results directly elucidate how the modifications in network morphology affect the origin of the elastic properties.

Our results confirm that the macroscopic network elasticity is directly related to structural parameters measured at the length scale of the mesh size, typically <1 $\mu$m, over a large range of cross-link densities, bundle thicknesses and filament densities. They also suggests that the mechanical properties of the network should be invariant from micro to macroscopic length scales; this is confirmed by our data showing that the elastic moduli obtained from both the 1-P and 2-P microrheology are comparable with the bulk network modulus (see Fig. 5-4).

In summary, we show that the linear elasticity of the actin-scruin composite network can be directly related to the properties of an individual bundle and its structural organization. The rigid, inextensible and irreversible cross-linking provided by scruin enables us to simplify the composite system by ignoring the effects of single molecule elasticity of the cross-linkers. Thus, the actin-scruin composite network is an excellent model system with which to study the physics of semi-flexible biopolymer networks. The results presented in our paper provide new tools to measure both the microscopic structure and the elastic properties of the network over a wide range of length scales, and new insights into the relationship of the mechanical properties of the disordered network to changes in its microstructure and organization.

# Chapter 6

# Conclusion

## 6.1 Summary

In this work, we investigated dynamics and statics of both ordered and disordered actin assemblies composed of identical constituent proteins, actin, scruin, and CaM. The ordered *in vivo* actin:scruin complex is found in the sperm of horseshoe crabs and undergoes a dynamic transformation from a coil to a straight bundle. To identify the basis for this movement, we examined the possible sources of chemical and mechanical energy involved during the reaction, and showed that the coil releases approximately $10^{-13}$ J of stored mechanical strain energy from the filament twists while chemical energy derived from calcium binding is only approximately $10^{-15}$ J. We also showed that the extension of the initially coiled actin bundle occurs at a constant velocity, leading to a hypothesis that the process must proceed like a zipper wherein a small region of the coiled bundle untwists initially and this conformational change then propagates along the bundle. This localized uncoiling would give rise to an incremental energy release, corresponding to a constant force generation during the reaction. The generated force of this dynamic actin spring was measured by embedding sperm cells in a solid block of agarose and triggering them to react inside agarose. The extending acrosomal bundle travels against a shear drag exerted by the agarose until the opposing drag force exceeds the force produced by the acrosome. The stalling yielded an upper bound estimate of the actin spring force, which is sufficiently large to successfully penetrate a tough jelly coat of a *Limulus* egg whose required puncturing

force is 0.8 nN for the acrosome tip of 48nm in diameter. Therefore, we confirm that scruin mediated crystalline bundle of actin filaments *in vivo* functions as a dynamic mechanical spring, representing a third type of actin-based motility that is distinctly different from the better known polymerization or myosin-driven processes.

*In vitro*, on the other hand, actin filaments polymerized in the presence of scruin form an isotropic, disordered three-dimensional semi-flexible network of cross-linked and bundled F-actin. Unlike ordered crystals, disordered networks often exhibit a complex relationship between their macroscopic mechanical properties and the elastic properties of the constituent filaments. While the biological significance of the actin binding proteins is well documented, little is known about how bundling and cross-linking quantitatively affect the microstructure and mechanical properties of actin networks. In this work, we quantified the effect of an ABP, scruin, on actin networks using imaging techniques, co-sedimentation assays, multi-particle tracking and bulk rheology. We showed how the structure of the actin network is modified as the scruin concentrations is varied, and we correlated these structural changes to variations in the resultant network elasticity. Due to the rigid, inextensible and irreversible cross-linking provided by scruin, the actin-scruin composite network is an excellent model system with which to study the physics of semi-flexible biopolymer networks. The results presented in this work provide new tools to measure both the microscopic structure and the elastic properties of the network over a wide range of length scales, and new insights into how the mechanical properties of the disordered network are related to changes in its microstructure and organization.

## 6.2 Future outlook

Next step from our current research is to investigate a way to form an isolated crystalline *in vitro* bundle that is similar to what we find *in vivo*. In collaboration with Margaret Gardel from Dave Weitz lab in the department of Physics at Harvard University, we are interested in measuring the force generated during a polarized growth of bundled actin filaments. From a pool of actin monomers and actin bundling proteins such as scruin, fambrin, or fascin, we can produce a bundle of highly organized

actin filaments. Miyata and Hotani have observed morphological changes in liposome caused by polymerization of encapsulated actin [36]. Also, D. Fygenson measured force generated as encapsulated microtubules buckle to deform lipid vesicles [17]. Thus, we may utilize these observations and experimental techniques to measure the force generated by growing an actin bundle inside a lipid vesicle. To construct an actin bundle like that of the true discharge, we can use fragments of purified true discharge as templates from which the bundled actin filaments can initiate their growth. Initial step in this project will be to find a suitable protocol to encapsulate the monomeric actin and actin binding proteins. Furthermore, ideally we would like to be able to synthesize a coiled actin bundle to be used as a molecular actuator.

# Bibliography


[1] F. Amblard, B. Yurke, A. Pargellis, and S. Leibler. A magnetic manipulator for studying local rheology and micromechanical properties of biological systems. *Rev. Sci. Instrum.*, 67(3):818–827, 1996.

[2] J. Andre. A propos d'une lecon sur la limule. *Ann. Fac. Sci. Clermont.*, 26:27–38, 1965.

[3] J. R. Bartles. Parallel actin bundles and their multiple actin-bundling proteins. *Curr. Opin. Cell Biol.*, 12:72–78, 2000.

[4] A. R. Bausch, W. Moller, and E. Sackmann. *Biophys. J.*, 76:573–579, 1999.

[5] D. Bray. *Cell Movements.* Garland Publishing, INC, 1992.

[6] K. Cant, B. A. Knowles, M. S. Mooseker, and L. Cooley. Drosophila singed, a fascin homolog, is required for actin bundle formation during oogenesis and bristle extension. *J. Cell Biol.*, 125:369–380, 1994.

[7] C. S. Cohan, E. A. Welnhofer, L. Zhao, F. Matsumura, and S. Yamashiro. Role of actin bundling protein fascin in growth cone morphogenesis: localization in filapodia and lamellipodia. *Cell Motility and the Cytoskeleton*, 48:109–120, 2001.

[8] J. C. Crocker, M. T. Valentine, E. R. Weeks, T. Gisler, P. D. Kaplan, A. G. Yodh, and D. A. Weitz. Two-point microrheology of inhomogeneous soft materials. *Phys. Rev. Lett.*, 85:888–891, 2000.

[9] J.C. Crocker and D.G. Grier. Methods of digital video microscopy for colloidal studies. *Journal of Colloid and Interface Science*, 179:298–310, 1996.

[10] B. R. Dasgupta, S. Y. Tee, J. C. Crocker, B. J. Frisken, and D. A. Weitz. Microrheology of polyethylene oxide using diffusing wave spectroscopy and single scattering. *Phys. Rev. E*, 65:051505–051515, 2002.

[11] D. DeRosier. How to build a bend into an actin bundle. *J. Mol. Biol.*, 175:57–73, 1984.

[12] D. DeRosier, L. Tilney, and P. Flicker. A change in the twist of the actin-containing filaments occurs during the extension of the acorosomal process in *limulus* sperm. *J. Mol. Biol.*, 137:375–389, 1980.

[13] D. DeRosier, L. G. Tilney, E. M. Bonder, and P. Frankl. A change in twist of actin provides the force for the extension of the acrosomal process in limulus sperm: the false-discharge reaction. *J. Cell Biol.*, 93(2):324–37, 1982.

[14] E. H. Egelman and D. J. DeRosier. Image analysis shows that variations in actin crossover spacings are random, not compensatory. *Biophy. J.*, 65(5):1299–1305, 1992.

[15] E. H. Egelman, N. Francis, and D. J. DeRosier. F-actin is a helix with a random variable twist. *Nature*, 298:131–135, 1982.

[16] B. Fabry, G.N. Maksym, J.P. Butler, M. Glogauer, D. Navajas, and J. J. Fredberg. I don't know yet. *Phys Rev. Lett.*, 87:1481021–1481024, 2001.

[17] D.K. Fygenson. *Microtubules: The rythm of assembly and the evolution of form.* PhD thesis, Princeton University, 1995.

[18] M. L. Gardel, M. T. Valentine, J. C. Crocker, A. R. Bausch, and D. A. Weitz. *Phys. Rev. Lett.*, 91:158302, 2003.

[19] M. B. Heintzelman and M. S. Mooseker. Assembly of the brush border cytoskeleton: changes in the distribution of microvillar core proteins during enterocyte differentiation in adult chicken intestine. *Cell Motil. Cytoskel.*, 15:12–22, 1990.

[20] B. Hinner, M. Tempel, E. Sackmann, K Kroy, and E. Frey. Entanglement, elasticity, and viscous relaxation of actin solutions. *Phys. Rev. Lett.*, 81:2614, 1998.

[21] H. Hotani. Micro-video study of moving bacterial flagella filaments ii: polymorphic transitions. *Biosystems*, 12:325–330, 1982.

[22] J. Howard. *Mechanics of Motor Proteins and the Cytoskeleton.* Sinauer Associate, Inc., Sunderland, MA, 2000.

[23] H. Isambert, P. Venier, A.C. Maggs, A. Fattoum, R. Kassab, D. Pantaloni, and M. F. Carlier. Flexcibility of actin filaments derived from thermal fluctuationsj. biol. chem. *J. Biol. Chem.*, 270(19):11437–11444, 1995.

[24] P. A. Janmey, S. Hvidt, J. Lamb, and T. P. Stossel. *Nature*, 345:89–92, 1990.

[25] M. Keller, J. Schilling, and E. Sackmann. Oscillatory magnetic bead rheometer for complex fluid microrheometry. *Rev. Sci. Inst.*, 72:3626–3634, 2001.

[26] H. Kojima, A. Ishijima, and T. Yanagida. Direct measurement of stiffness of single actin filaments with and without tropomyosin by in vitro nanomanipulation. *Proc. Natl. Acad. Sci., USA*, 91:12962–12966, 1994.

[27] T. Kreis and R. Vale. *Guidebook to the cytoskeletal and motor proteins, 2nd eds.* Oxford University Press, New York, 1999.

[28] L. D. Landau and E. M. Lifshitz. *Theory of Elasticity, 3rd ed.* Pergamon, Inc, 1986.

[29] R. W. Lymn and E. W. Taylor. Micro-video study of moving bacterial flagella filaments ii: polymorphic transitions. *Biosystems*, 10(25):4617–4624, 1971.

[30] F. C. MacKintosh, J. A. Kas, and P. A. Janmey. Elasticity of semi- flexible biopolymer networks. *Phys. Rev. Lett.*, 75:4425–4428, 1995.

[31] L. Mahadevan and P. Matsudaira. Motility powered by supramolecular springs and ratchets. *Science*, 288(5463):95–100, 2000.

[32] L. Mahadevan, C. Riera, and P. Matsudaira. Dynamics paper. submitted to, 2003.

[33] T. G. Mason and D. A. Weitz. Optical measurements of frequency-dependent linear viscoelastic moduli of complex fluids. *Phys. Rev. Lett.*, 74:1250–1258, 1995.

[34] P.T. Matsudaira and D.R. Burgess. Identification and organization of the components in the isolated microvillus cytoskeleton. *J. Cell Biol.*, 83:667–673, 1979.

[35] J. L. McGrath, J. H. Hartwig, and S. C. Kuo. The mechanics of f-actin microenvironments depend on the chemistry of probing surfaces. *Biophysical Journal*, 79:3258–3266, 2000.

[36] H. Miyata and H. Hotani. Morphological changes in liposomes caused by polymerization of encapsulated actin and spontaneous formation of actin bundles. *Proc. Natl. Acad. Sci. USA*, 89:11547–11551, 1992.

[37] D. C. Morse. Viscoelasticity of concentrated isotropic solutions of semiflexible polymers. 2. linear response. *Macromolecules*, 31:7044–7067, 1998.

[38] F. R. N. Nabarro. *Theory of crystal dislocations.* Oxford University Press, 1967.

[39] F. Oosawa and S. Asakura. *Thermodynamics of the polymerization of protein.* Academic Press, Inc, 1975.

[40] R. Ruddies, W. H. Goldmann, G. Isenberg, and E. Sackmann. *Euro. Biophys. J. Biophys. Lett.*, 22:309–321, 1993.

[41] M. C. Sanders, M. Way, J. Sakai, and P. Matsudaira. Characterization of the actin cross-linking properties of the scruin- calmodulin complex from the acrosomal process of limulus sperm. *J. Biol. Chem.*, 271:2651–2657, 1996.

[42] M.F. Schmid, J.M. Agris, J. Jakana, P. Matsudaira, and W. Chiu. Three-dimensional structure of a single filament in the limulus acrosomal bundle: Scruin binds to homologous helix-loop beta motifs in actin. *J. Mol. Biol.*, 294:139–149, 1994.

[43] M.F. Schmid, P. Matsudaira, T. W. Jeng, J. Jakana, E. Towns-Andrews, J. Bordas, and W. Chiu. Crystallographic analysis of acrosomal bundle from limulus sperm. *J. Mol. Biol.*, 221:711–725, 1991.

[44] B. Schnurr, F. Gittes, F. C. MacKintosh, and C. F. Schmidt. *Macromolecules*, 30:7781–7792, 1997.

[45] L. A. Selden, H. J. Kinosian, J. E. Estes, and L. C. Gershman. Impact of profilin on actin-bound nucleotide exchange and actin polymerization dynamics. *Biochemistry*, 38(9):02769–02778, 1999.

[46] A. N. Semenov. *J. Chem. Soc. Faraday Trans.*, 82:317, 1986.

[47] M.B. Sherman, J. Jakana, S. Sun, P. Matsudaira, W. Chiu, and M. F. Schmid. The three-dimensional structure of a dynamic actin bundle, the limulus acrosomal process. *J. Mol. Biol.*, 294:139–149, 1999.

[48] J. H. Shin, L. Mahadevan, P. So, and P. Matsudaira. Bending stiffness of a crystalline actin bundle. submitted to J. Mol. Biol., 2003.

[49] J. H. Shin, L. Mahadevan, G. Waller, K. Langsetmo, and P. Matsudaira. Stored elastic energy powers the 60$\mu$m extension of the *limulus* actin bundle. *J. Cell Biol.*, 162(7):1183–1188, 2003.

[50] R. L. Shoger and G. G. Brown. Ultrastructural study of sperm-egg interactions of the horseshoe crab *limulus polyphemus l. (merostomata: xiphosura). J. Submicr. Cytol.*, 2:167–179, 1970.

[51] S. Sun, M. Footer, and P. Matsudaira. Modification of cys-837 identifies an actin-binding site in the b-propeller protein scruin. *Mol. Biol. Cell*, 8:421–430, 1997.

[52] M. Tempel, G. Isenberg, and E. Sackmann. *Phys. Rev. E*, 54:1802–1810, 1996.

[53] L. G. Tilney. Actin filaments in the acrosomal reaction of limulus sperm. motion generated by alterations in the packing of the filaments. *J. Cell Biol*, 64(2):289–310, 1975.

[54] L. G. Tilney. Actin filaments, stereocilia and hair cells: how cells count and measure. *Annu. Rev. Cell Biol.*, 8:257–274, 1992.

[55] L. G. Tilney, J. G. Clain, and M. S. Tilney. Membrane events in the acrosomal reaction of *limulus* sperm. *J. Cell Biol.*, 81:229–253, 1979.

[56] L. G. Tilney, P. Connelly, S. Smith, and G. M. Guild. F-actin bundles in drosophila bristles are assembled from modules composed of short filaments. *J. Cell Biol.*, 135:1291–1308, 1996.

[57] L. G. Tilney, D. DeRosier, and M. J. Mulroy. The organization of actin filaments in the stereocilia of cochlear hair cells. *J. Cell Biol.*, 86:244–259, 1980.

[58] L. G. Tilney, M. S. Tilney, and G. M. Guild. F-actin bundles in drosophila bristles. i. two filament cross-links are involved in bundling. *J. Cell Biol.*, 130:629–638, 1995.

[59] M. S. Tilney, L. G. Tilney, R. E. Stephens, C. Merte, D. Drenckhahn, D. A. Cotanche, and A. Bretscher. Preliminary characterization of the stereocilia and cuticular plate of hair cells in the chick cochlea. *J. Cell Biol.*, 109:1711–1723, 1989.

[60] M. T. Valentine, P. D. Kaplan, D. Thota, J. C. Crocker, T. Gisler, R. K. Prud'homme, M. Beck, and D. A. Weitz. Investigating the microenvironments of inhomogeneous soft materials with multiple particle tracking. *Phys. Rev. E*, 64:061506–061515, 2001.

[61] M. T. Valentine1, Z. E. Perlman, M. L. Gardel, , P. Matsudaira J. H. Shin, T. J. Mitchison, and D. A. Weitz. Colloid surface chemistry critically affects multiple particle tracking measurements of biomaterials. submitted to Biophycal Journal, 2003.

[62] N. Volkmann, D. DeRosier, P. Matsudaira, and D. Hanein. An atomic model of actin filaments cross-linked by fimbrin and its implications for bundle assembly and function. *J. Cell Biol.*, 153:947–956, 2001.

[63] D. Wachsstock, W. Schwarz, and T. Pollard. Affinity of alpha-actinin for actin determines the structure and mechanical properties of actin filament gels. *Biophy. J.*, 65:205–214, 1993.

[64] D. Wachsstock, W. Schwarz, and T. Pollard. Cross-linker dynamics determine the mechanical properties of actin gel. *Biophy. J.*, 66:801–809, 1994.

[65] A. Weber. Actin binding proteins that change extent and rate of actin monomer-polymer distribution by different mechanisms. *Mol Cell Biochem.*, 190:67–74, 1999.

[66] I. Y. Wong, M. L. Gardel, D. R. Reichman, E. R. Weeks, M. T. Valentine, A. R. Bausch, and D. A. Weitz. Anomalous diffusion probes microstructure dynamics of entangled f-actin networks. submitted to Phys. Rev. Lett., 2003.

[67] J. Wyman. Linked functions and reciprocal effects in hemoglobin: a second look. *Adv. Protein. Chem.*, 19:223–286, 1964.

[68] J. Y. Xu, D. Wirtz, and T. D. Pollard. Dynamic cross-linking by alpha-actinin determines the mechanical properties of actin filament networks. *J. Biol. Chem.*, 273(16):9570–9576, 1998.

[69] I. Yamashita and K. Namba. Structure and switching of bacterial flagellar filaments studied by x-ray fiber diffraction. *Nature Struct.*, 5:125–132, 1998.